MULTI-SCALE FATIGUE DAMAGE LIFE ASSESSMENT OF A RAILWAY WHEEL USING A CRITICAL-PLANE MODEL

A Dissertation

by

MAYSAM KIANI

Submitted to the Office of Graduate and Professional Studies of
Texas A&M University
in partial fulfillment of the requirements for the degree of

DOCTOR OF PHILOSOPHY

Chair of Committee,	Gary T. Fry
Committee Members,	Harry L. Jones
	Peter B. Keating
	Anastasia Hanifah Muliana
Head of Department,	Robin Autenrieth

May 2017

Major Subject: Civil Engineering

ABSTRACT

A 3D finite element model is constructed in ABAQUS® to simulate the stress/strain fields that take place under the rolling-contact of railway wheels on rails. This FE model constitutes a faithful replica of a railway wheel that is rolled on a rail segment using a hard-contact over-closure relationship and an elastoplastic material model with isotropic and kinematic hardening. This material model predicts the wheel's stabilized steady-state structural response using a multiaxial critical-plane fatigue model that accounts for the effect of residual stresses.

The steady-state stress/strain response of the wheel is post-processed using algorithms written in MatLab® to obtain state-of-the-art analytical predictions of subsurface micro-crack initiation within the railway wheel. Finally, based on the results obtained from the crack initiation study, a pre-cracked multiscale model is constructed to investigate the influence of a subsurface crack on the wheel's stress fields.

To my family

ACKNOWLEDGMENT

This research would not have been possible without the help of several people. First, I sincerely thank my committee chair, Dr. Gary Fry, who supervised this research and provided helpful suggestions and insightful directions in writing this dissertation. I feel extremely fortunate for the chance to be a part of his research group. I would also like to thank my committee members Dr. Harry Jones, Dr. Peter Keating, and Dr. Anastasia Muliana for their support throughout the course of this research.

Furthermore, I would also like to acknowledge the crucial role of Texas A&M Transportation Institute, Association of American Railroads, and Texas A&M Supercomputing Facility for funding the project and providing the resources during this research.

Last but not least, I would like to extend my sincere gratitude to my parents for their endless support during my stay at Texas A&M University.

CONTRIBUTORS AND FUNDING SOURCES

Contributors

This work was supported by a dissertation committee comprises Dr. Gary Fry, Dr. Harry Jones, and Dr. Peter Keating of the Civil Engineering department and Dr. Anastasia Muliana of Mechanical Engineering department.

All the work conducted for the dissertation was completed by the student independently.

Funding Sources

Graduate study was supported by dissertation research project grants from Texas A&M Center for Transportation Safety, American Association of Railroads, and university affiliated lab for railway research.

TABLE OF CONTENTS

Page

LIST OF FIGURES

Page

LIST OF TABLES

Page

1 INTRODUCTION

1.1 Introduction

Technological advancements in the railway industry have made it possible to significantly extend the wear life of wheels. Simultaneously, current economical and logistical constraints demand increasing train speeds and load capacities that result in larger contact forces acting on rails and wheels. As a result, longer wear periods, higher speeds, and larger loads have made fatigue the main cause of railway wheel replacement and re-engineering [1].

There are roughly 25-50 million railway wheels in operation in the world. Considering an annual failure rate of one in 1000, it means 25,000-50,000 wheel failures every year. It's obvious that if 'failure' here means a complete fracture of the wheel the way the train to be inoperative, railways would not be an efficient method of transportation [2].

According to the Union Pacific Railroad wheel fracture database, 65% of railroad wheel failures are caused by shattered rims [3], a form of subsurface initiated rolling-contact fatigue (RCF). This suggests a need for the development of models that can effectively predict RCF cracks. Effective predictions require computational tools and mathematical models that can accurately simulate actual material behavior and structural interactions due to contact between railway wheels and rails.

Wheels constitute a fundamental component in railways; without them, the directed motion of the railway wagons and their contents is not possible. While there are

many other components in trains that are as crucial as wheels for the transport of goods and/or people, the strategic location and function of wheels make them a component that is also critical to safety. That is, failures in other primary components of railways, such as the engine, may not necessarily represent a safety threat to the contents of the cars. The failure of wheels, which is structural in nature, can seriously compromise the integrity of the transport medium. The inability of railway wheels to resist the loads they are subjected to while in service can eventually result in damage to rails, sleepers, the train's suspension, and/or bearings, and in some cases, can even result in derailments. The consequences of these types of damage can be both costly and endangering to humans.

Fatigue-damage in railway wheels is manifested as follows:

1. Fatigue at the rolling surface favored by local (cyclic) plastic behavior, presence of liquids in cavities, corrosion, rolling surfaces asperities, geometrical defects, material defects, and thermal loading [4].
2. Subsurface fatigue favored by (cyclic) plastic behavior, thermal loading, geometrical defects, and material defects [5], and
3. Fatigue at deep defects caused by the stress magnification that occurs due to these defects.

As is made evident by the above list, all modes of failure are the result of, among other factors, a combined action of (cyclic) plasticity and thermal loading. Plasticity is the result of mechanical loads that arise from the large contact forces occurring between wheels and the rail. These loads are imposed by the weight of the railway cars and amplified by the motion of the train taking place on the imperfect rolling surfaces of both

the rail and wheels. Thermal loads, in turn, are caused by the continuous friction between the wheels and the rail. An important increase in the wheels' temperature is induced by slipping, which is related directly or indirectly to the action of the brakes. During braking, slipping of the surface of the wheel can occur between the wheel and the rail and/or between the wheel and the brake blocks in railways that incorporate this latter type of brake system. The cyclic nature of the loads acting on railway wheels results from their rolling, in the case of mechanical loads, and from their heating and subsequent cooling that takes place during and after braking.

Studies on the fatigue of rails are abundant; just a few samples of these include the development of pertinent fatigue models [6], of fatigue crack models [7], the study of the mechanisms of crack initiation [8], the contributions of residual stresses [8], attempts to predict their fatigue-life [9]the consideration of surface imperfections [10], the evaluation of surface treatments [11, 12], and the use of different grade steels and steel manufacturing techniques [13-15].

1.2 Objectives and Organization

The objective of this study is to provide a relatively accurate numerical prediction of subsurface crack initiation (location and orientation) of a 'defect-free' wheel as well as the number of cycles required for the micro-cracks to nucleate using a strain-based critical-plane model. The same wheel also analyzed with the presence of a crack to investigate the behavior of a defect at subsurface level of a railway wheel.

Section 2 presents a full-scale computer simulation of wheel-rail contact with a non-linear isotropic/kinematic hardening material. Section 3 presents a multiaxial fatigue analysis of a wheel section as a result of rolling contact using a strain-based critical-plane model to predict life-to-crack-initiation of wheels. Section 4 presents implementation of a subsurface crack in the same wheel model using sub-modeling technique to investigate the effect of a defect on the wheel's stress-strain fields at subsurface level. Finally section 5 presents the overall conclusions as well as suggestions for continuation of this study.

2 COMPUTER SIMULATION OF 'DEFECT-FREE' WHEEL-RAIL CONTACT

2.1 Introduction

Rolling contact fatigue (RCF) has been considered as one of the root causes of many derailment accidents [16, 17]. Kapoor [18] suggests that either low-cycle fatigue (LCF) or ratcheting is the failure mode of material in this region, e.g. their failure mechanisms are independent from each other. In contrast to surface cracks, subsurface cracks nucleate at some depth below running surface where material deforms elastically; typically, accompanying with a presence of material imperfections or discontinuities that may act as a stress intensifier. Another important factor that can significantly affect the crack growth rate and thereby affect the wheel fatigue life is residual stress in wheel rim which is investigated in this section. The shattered and vertical split rim (VSR) crack growth rates depend on the residual stresses in wheel rims [19].

The objectives of this section are: 1) to develop a full-scale finite element model of wheel-rail rolling contact with a nonlinear isotropic/kinematic hardening material model, 2) to predict residual stresses and strains at the wheel's subsurface level, 3) to provide an in-depth understanding of the state of stress and strain from wheel-rail contact phenomena and ratcheting behavior, 4) to study the influence of residual stresses on rolling stresses in term of fatigue damage. It should be noted that the effects from thermal-mechanical coupling due to braking or heat transfer during service are not considered in this study.

2.2 Background

Rolling-contact fatigue is different from classical fatigue in the following aspects [20]:

- Rolling causes a non-proportional and out-of-phase multiaxial state of stress;
- Cracks propagate in mixed modes II and III;
- Friction between opposite crack-faces plays an important role in the rate of crack-propagation; and
- Because of the multiaxial stress field, specialized fatigue models should be employed, since traditional models have been developed for tensile loading.

Previous attempts to predict the initiation and propagation of fatigue-cracks in defect-free materials under rolling-contact have resorted to a series of theoretical assumptions and analytical simplifications. Among the most popular simplifications are: the use of Hertzian contact theory [21], 2-D analytical schemes, elastic material assumptions, and (uniaxial) stress-life fatigue models. Hertzian contact theory assumes that:

1. The material behaves elastically,
2. The contact surfaces are continuous and non-conformal
3. The contact area is much smaller than the characteristic radii of the bodies in contact,
4. Friction is negligible, and
5. The object is a continuum.

Analytical solutions of the existing contact stress field based on Hertzian theory are relatively easy to determine provided the problem satisfies the assumptions in the

theory. However, this must rarely be the case in a railway wheel rolling on a rail since first, during rolling, a portion of the wheel typically responds inelastically. Second, the contact surfaces are conforming, and although the contact-area is indeed relatively small, its size is not negligible (compared to the dimensions of the bodies in contact). Furthermore, friction plays a vital role in the rolling process of the wheel and is responsible for the induction of shear stresses in the wheel that, in turn, are responsible for the nucleation of fatigue cracks; therefore, friction cannot be ignored if accurate results are desired.

With respect to the fatigue models, when it comes to the analysis of the subsurface RCF within railway wheels, the bodies in contact are in a multiaxial stress state. Multiaxial fatigue theory is therefore needed to make accurate fatigue-initiation-life predictions. In recognition of this, the Dang Van multiaxial equivalent-stress fatigue criterion has become a common resource. This criterion constitutes a mesoscopic approach that has only rarely been successfully compared to multiaxial fatigue tests [22]. Part of its lack of success may be due to the fact that it constitutes a stress-life approach, whereas in wheel-rail contact, a region of plastic behavior is generally present, which demands the use of strain-life approaches for closer-to-reality results.

2.3 Description of Rolling Contact Fatigue in Railway Wheels

The roots of the RCF problem in wheels have been identified above, together with the mechanisms that cause an initial crack to induce structural failure of a wheel. Three different regions where fatigue can initiate have been identified; their differences stem from the causes that trigger the development of the fatigue processes. The three re-

gions are: the tread surface, a subsurface region that ranges from about 3 to 10 mm in depth, and one more that is located primarily between 10 and 30 mm below the surface of the wheel.

2.3.1 Fatigue at the Wheel Tread

Fatigue at the wheel tread, also called surface fatigue, is influenced by both mechanical and thermal loading [3]. Stresses can be very high at the immediate wheel-rail contact region, and together with the friction forces that are induced during rolling, they can cause the material to undergo increasingly severe plastic deformations with every revolution of the wheel. This phenomenon, known as ratcheting, can occur even under moderate axle-loads, causing the stresses and strains to exceed the elastic limits of the material and accumulate with each load cycle. If ratcheting occurs continuously, it can cause local fractures in the material at regions where the stresses eventually reached the fracture strength of the material (Figure 2.1). These local cracks can develop into global fractures over time.

Cracks initiated by the local plasticity of the wheel surface tend to propagate in the circumferential direction until they result in the separation of material from the wheel in the form of chips [23]. Normally, this type of failure (shelling) does not represent immediate danger; however, it affects the smooth rolling of the wheels. If left unrepaired, the impact of the loss of surface curvature can lead to serious damage in the wheel and/or the rail.

Figure 2.1. Damage within the wheel tread resulting from surface cracks [4]

Thermal loads also cause fatigue cracks at the surface of the wheel due to softening or weakening of the material's resistance to cyclic straining. Furthermore, rapid cyclic fluctuations in the tread's temperature may lead to material phase transformations and the formation of zones of martensite, which exhibits smaller resistance to fatigue caused by a brittle mode of failure. An example of a failure related to rapid changes in material temperature is the so-called wheel flat [4]. Here, relatively rapid heating of the wheel due to breaking/slipping is followed by cooling of the material via heat transfer to the surrounding air. This produces zones of martensite that eventually develop into crack-initiation sites that may lead to major detachments of material from the wheel. Less serious thermally-initiated cracks result in the separation of small material fragments from the wheel tread, which is known as shelling. The effects of both shelling and spalling (Figure 2.2) represent a significant cost to the railway industry. In order to re-

duce these effects, Diener and Ghidini [24] have proposed criteria for the design of new materials for railway wheels as well as maintenance measures such as wheel re-profiling. As with the grinding procedure in rails, this procedure prevents the development of crack networks and cavities around the perimeter of the wheel.

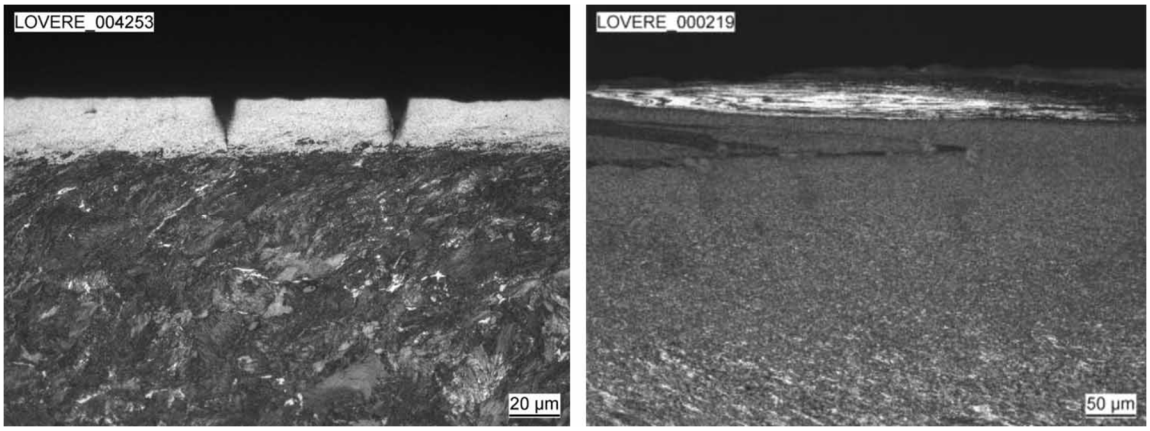

Figure 2.2. Spalling in wheels due to thermal cracking [24]

2.3.2 Subsurface Fatigue

In ‘defect-free’ wheel steels, crack initiation below the surface tends to take place at approximately 3 to 10 mm below the wheel rolling-surface [6], where the largest shear stresses due to rolling occur. When the fatigue process is initiated within this region, it is known as subsurface fatigue. By ’defect-free’, it is meant that the actual conditions of the wheel material (in terms of cast-in defects and inclusions) correspond to or are better than those present in the test samples used in the determination of the fatigue properties of that material. In other words, although microscopic flaws are unavoidable, they have already been implicitly taken into account in the ‘defect-free’ characterization of the ma-

terial so that there is no need to apply additional reductions to the nominal fatigue-resistance.

Ekberg and Kabo [25] have categorized subsurface fatigue crack in wheels into shallow and deep initiation mechanism. At shallow initiation of fatigue cracks in wheels, the crack typically grows downward towards the wheel hub in the subsequent propagation, as in Figure 2.3(a). It then deviates at a depth of some 20mm with a continuous growth in the circumferential direction. When initiated at a larger depth, the crack typically continues to grow at this depth, Figure 2.3(b). Final fracture will eventually occur as branching towards the surface as in Figure 2.3(a) or, more seldom, towards the wheel hub as in Figure 2.3(b).

In this subsurface region, although material plasticity and hardening may occur initially even at moderate load levels [20], at some point, the development of residual stresses may allow for the material to respond elastically in what is known as elastic shakedown. In regions of elastic shakedown, the fatigue phenomenon is of the high-cycle type. Cracks initiated in these regions end up propagating radially and may evolve into large detachments of the rim material, a phenomenon which is referred to as shattering. Measures to prevent shattering relate to the manufacturing processes of the wheels and their materials.

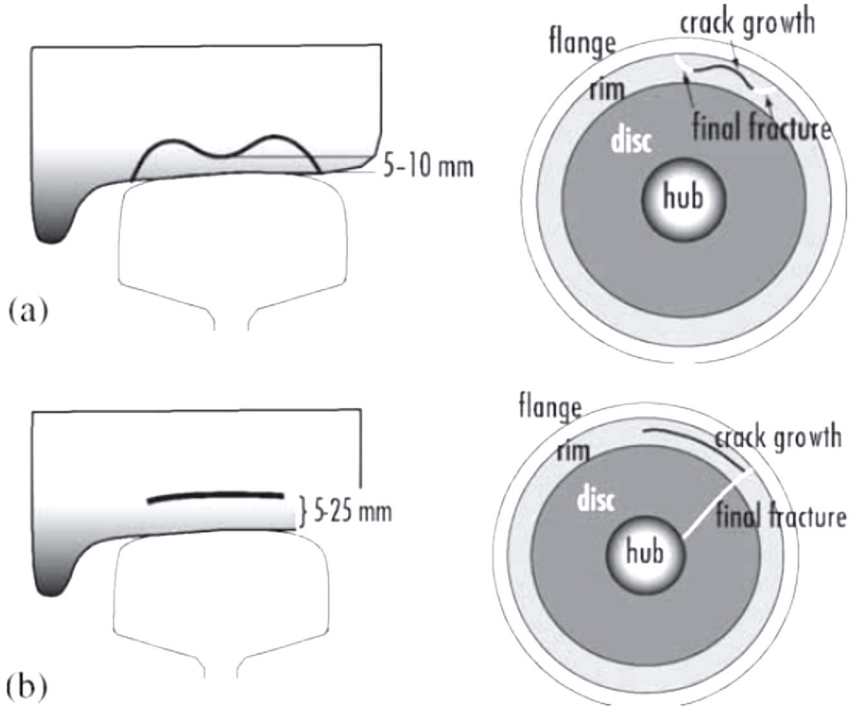

Figure 2.3. Typical appearance of subsurface fatigue cracks in railway wheels: (a) shallow initiation and (b) deep initiation at a defect [25]

2.3.3 Fatigue Initiated at Deep Defects

As will be shown later, the stress field that results from rolling-contact in wheels dies out significantly with depth so that deep crack-initiation (more than 10 mm in depth) can only take place in the presence of "macroscopic" defects that act as stress magnifiers [1]. These defects, if large enough, can propagate quite far from the contact region [22].

Macroscopic defects play the same role as already-initiated cracks. Studies on the effects of the presence of macroscopic defects have included the use of equivalent stresses [26], fracture mechanics [27], and finite element models [28, 29].

Finally, material related factors that have been shown to affect the fatigue-life in wheels are: the presence of hydrogen, chemical composition, metallography, grain size and texture, microstructure, mechanical properties, hardness, impact toughness, fatigue strength, anisotropy, etc. To increase the material fatigue endurance, engineering strategies attempt to decrease the sizes of inclusions, and improve their stability, material structure, and fatigue strength.

2.4 Engineering Assessments of Subsurface Fatigue

Microscopy of RCF defects have shown that fatigue may start as microscopic defects at depths of 3-4 mm below the tread surface (Figure 2.4), a zone where plasticity and wear represent competing damaging mechanisms, i.e., wear may remove material regions where cracks have nucleated.

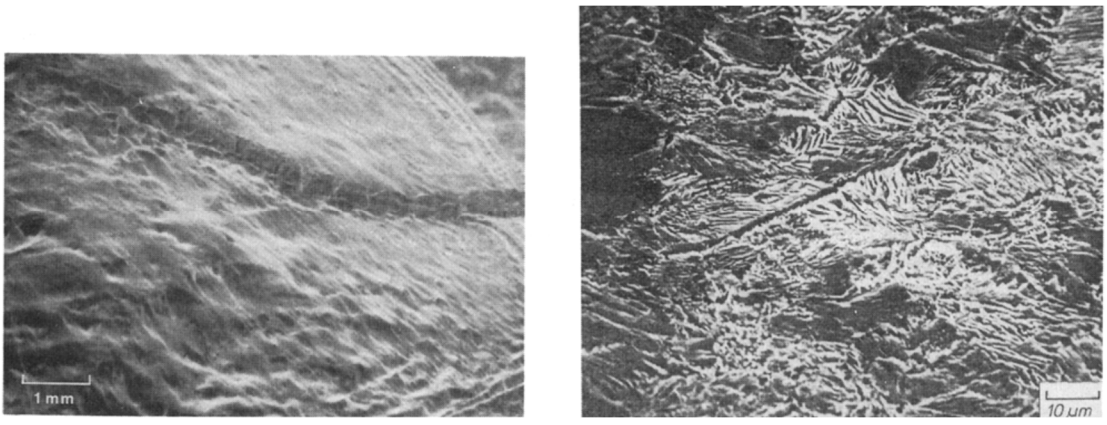

Figure 2.4. (a) RCF initiation in AAR class C wheel material, (b) micro-cracking in defective pearlitic steel [23]

Metallographic examinations like these suggest that shear cracking is responsible for RCF crack initiation once it exceeds fatigue-crack growth thresholds under the combined influence of normal and tangential forces [23]. In the subsurface, crack initiation is the rate-controlling step in RCF.

Despite the existence of these micro-cracks, to be able to use multiaxial fatigue criteria for the assessment of subsurface fatigue, the material is usually assumed to be 'defect-free'. Multiaxial fatigue criteria can be grouped into damage parameters and critical-plane approaches [30]. The damage parameters form a reference value averaged over all material planes of a material volume element. Energy-based approaches are an example of damage parameters. Some critical-plane approaches will be presented later in more detail.

Another way to categorize multiaxial fatigue theories is according to the physical quantity used in the theory. Thus, the theories can be classified as stress-based, strain-based, energy-based, and fracture mechanics-based. The stress-based approaches are limited to the high-cycle fatigue (HCF) regime where plastic strains are negligible. Strain-based approaches, on the other hand, can cover both low-cycle fatigue (LCF) and HCF regimes.

2.4.1 The Dang Van Fatigue Criterion

Dang Van, et al. [31] proposed an endurance limit criterion based on the concept of micro-stress within a critical volume of the material, which assumes that elastic shakedown occurs before the fatigue limit is reached and that mesoscopic and macro-

scopic plastic strains and residual stresses have been stabilized. The model resulted from the observation that fatigue-crack nucleation is a local process and begins in grains that have undergone plastic deformations and form slip bands. It is considered that, because cracks nucleate along these bands, the local shear stresses must have a relevant influence. Similarly, it is assumed that local hydrostatic stresses will have an effect on the mode I propagation of the cracks. The simplest version of the Dang Van fatigue criterion is given by [32]:

$$\tau(t) + a\sigma_h(t) = b \tag{2.1}$$

where $\tau(t)$ and $\sigma_h(t)$ are instantaneous microscopic shear stresses and hydrostatic stresses (to be defined below), a is a material constant and b is an equivalent-stress value related to fatigue-crack initiation in the material. The material constants a and b are determined for different fatigue life ranges.

A stress analysis of a loading cycle combined with a residual-stress analysis is required to obtain the microscopic stresses. The corresponding expression is [32]:

$$\sigma_{ij}(t) = \Sigma_{ij}(t) + \mathrm{dev}\rho^* \tag{2.2}$$

where Σ_{ij} is the macroscopic stress tensor, and dev ρ^* is the deviatoric part of the stabilized residual stress tensor. The microscopic shear stress is computed from the microscopic principal stresses using the Tresca maximum shear stress theory as:

$$\tau(t) = \frac{1}{2}\left[\sigma_1(t) - \sigma_3(t)\right] \tag{2.3}$$

2.4.2 Critical-plane Approaches

Some materials can experience additional hardening for out-of-phase or non-proportional loading meaning that under strain-controlled conditions, stresses in the material are higher for out-of-phase loading than for in-phase loading. These additional stresses can cause an accelerated amount of fatigue damage on critical planes as compared to in-phase loading. For fatigue calculations, constitutive models that do not account for non-proportional hardening effects may result in non-conservative fatigue life calculations [33].

In cases with plastic deformation, stress is not a reliable measure of the loading effect on fatigue life considering that a small increase in stress will result in a large increase in strain. Therefore, strain-based criteria may be adopted [20].

An early strain-based critical plane approach was proposed by Kandil, et al. [34], who proposed that a combination of shear strain and normal strain acting on a plane was responsible for crack initiation and growth:

$$\frac{\Delta\gamma_{max}}{2} + S\varepsilon_n = C \tag{2.4}$$

where

$\Delta\gamma_{max}/2 =$ the strain amplitude on the maximum shear strain plane

$\varepsilon_n =$ the normal strain on this plane

$S =$ a material fitting constant

This parameter provided a physical basis for crack growth for shear cracks opened by normal strains perpendicular to the crack surface. However, it has been shown by Socie and coworkers [32, 35] that strain parameters alone cannot correlate fatigue behavior for a range of materials subjected to both in-phase and out-of-phase loading.

The advantages of the critical plane approach for strain-based fatigue analysis mare the same as in the stress-based approach. The approach is general enough to apply to both proportional and non-proportional multiaxial loading conditions. The physical nature of the development of small cracks can be captured by the use of appropriate damage parameters. The expected crack orientation in the material can be calculated. However, an accurate constitutive model is essential in obtaining the best results, as is knowledge about the appropriate damage parameter to use for a given material at a particular load level [33].

Critical-plane approaches have been proposed for fatigue analysis of components with non-proportional multiaxial loading [36]. Non-proportional loading results in the rotation of the principal stress axes as well as the maximum shear stress/strain amplitude planes at a given material point. Cracks are expected to eventually initiate on planes and at material points where a particular fatigue-damage parameter is maximized during a load cycle. It is a fundamental task in critical-plane approaches to search for the plane(s) that displays the highest fatigue damage at several or, ideally, all of the material points in a structural component during a loading cycle.

Critical-plane models evolved from experimental observations of the crack-initiation and growth patterns in solids under cyclic loading. Experimental results show

that for commonly used metallic materials, fatigue crack first occurs along the crystal slip and then propagates perpendicular to the maximum principal stress direction. As it is illustrated in Figure 2.5, the fatigue fracture plane is the crack plane observed at the macro level, and critical plane is a material plane on which the fatigue damage is evaluated [37].

Critical-plane models should incorporate accurate constitutive parameters governing crack-initiation and growth so that they can successfully predict the fatigue-life and the orientation of the failure planes. Because different materials possess different failure modes, adequate models have to be employed to achieve accurate fatigue-life predictions in all life regimes.

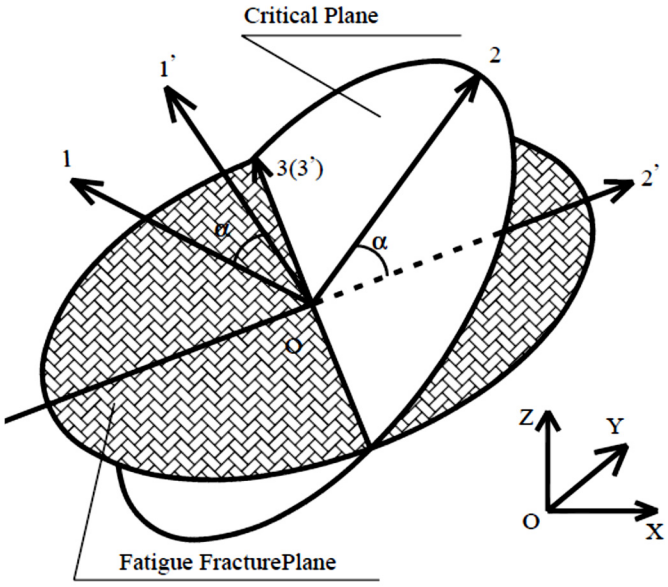

Figure 2.5. Relationship between the critical and fatigue fracture planes [3]

2.5 Wheel-Rail Rolling-Contact Stress Analysis

Most fatigue models rely on stress and strain input values to produce their predictions. In this study, time-history contact-stress analyses of a railway wheel rolling on a rail segment are performed using a 3-D FE model. The results of these analyses are later used in a multiaxial strain-based fatigue model to estimate the location and orientation of the first subsurface fatigue crack as well as the number of cycles required to initiate it. The details of the constructed FE model are described in the following subsections.

2.5.1 Material Model

2.5.1.1 Response of Material Subjected to Cyclic Loading

In wheel/rail contact, plastic deformation will usually occur even at fairly moderate load levels [20]. Plastically deformed material experiences plastic hardening as well as accumulation of residual stresses. Due to these two effects, a load magnitude that causes plastic deformation may, after some load cycles, only cause elastic response. This effect called *elastic shakedown*. With a more severe loading, the cyclic stress train curve becomes a stabilized closed loop with zero total plastic deformation. Such material response called *plastic shakedown*. Finally, when every load cycle causes additional plastic deformation and the deformation exceeds the material ductility, the material response called *ratchetting* or cyclic creep (Figure 2.6).

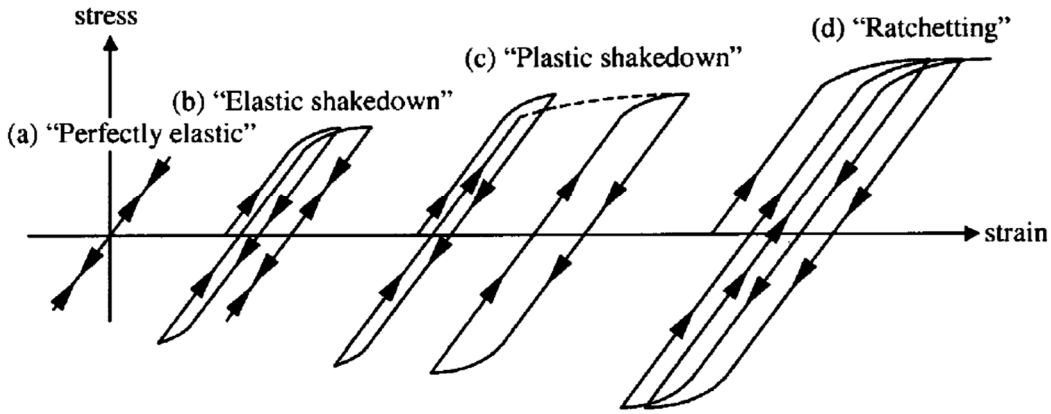

Figure 2.6. Illustration of different material responses that may occur for a material subjected to stress-controlled cyclic loading with a constant non-zero mean load [8]

2.5.1.2 Chaboche Plasticity Model and the Mechanical Properties of a Pearlitic Rail Steel

Due to heavy axle loads in locomotive industry, localized plastic deformation occurs at the wheel-rail contact interface [38]. Such a compressive deformation at running surface is balanced by tensile residual stresses at subsurface, which is found to play an important role in fatigue crack nucleation [39]. The stress-strain relationship for all of the components in the FE model is defined using a plasticity model with both isotropic and kinematic hardening [40].

Johansson and Thorbemtsson [41] developed an optimization algorithm - based on Bower [42] test results on rail steels – to calibrate parameters for Chaboche plasticity model. The optimization result showed an accurate ratchetting prediction with some deviation of the shape in stress-strain plots. Using stress-strain plots of specific loading cycles, Ringsberg, et al. [8] later used this optimization results to determine Chaboche model parameters and implemented it into ABAQUS material library to study FEA of

rolling contact. Due to less complexity of Chaboche plasticity model, it is more suitable for studying FEA of computationally intensive full-scale wheel rail contact [39].

In general, isotropic and kinematic hardening rules are coupled in plasticity models. The isotropic hardening rule predicts change of the size of yield surface as plastic deformation evolves, while the kinematic hardening rule is responsible for the translation of yield surfaces—called *Bauschinger effect*—due to cyclic load. The kinematic hardening rule also controls the ratcheting behavior of material.

The yield criterion in the model uses the von Mises equivalent stress concept, according to which a material point is considered to reach its yield point when the second invariant of the deviatoric stress tensor at that point equals the square of the yield stress of the material. Thus, the yield surface is defined by:

$$F = \sqrt{\frac{3}{2}(\boldsymbol{S} - \boldsymbol{\alpha}^{dev}) : (\boldsymbol{S} - \boldsymbol{\alpha}^{dev})} - \sigma^0 = 0 \tag{2.5}$$

where $\boldsymbol{S}$ corresponds to the deviatoric stress tensor at the material point of interest and $\boldsymbol{\alpha}^{dev}$ to the deviatoric part of the back-stress tensor.

Kinematic hardening models assume associated plastic flow, which is given by:

$$\dot{\varepsilon}^{pl} = \dot{\bar{\varepsilon}}^{pl} \frac{\partial F}{\partial \boldsymbol{\sigma}} \tag{2.6}$$

where $\dot{\varepsilon}^{pl}$ is the rate of plastic flow and $\dot{\bar{\varepsilon}}^{pl}$ is the equivalent plastic strain rate. This latter is obtained from the performed plastic work,

$$\sigma^0 \dot{\bar{\varepsilon}}^{pl} = \boldsymbol{\sigma} : \dot{\boldsymbol{\varepsilon}}^{pl} \tag{2.7}$$

which yields $\dot{\bar{\varepsilon}}^{pl} = \sqrt{\frac{2}{3}\dot{\boldsymbol{\varepsilon}}^{pl} : \dot{\boldsymbol{\varepsilon}}^{pl}}$ for isotropic Mises plasticity. The kinematic hardening law is then given as:

$$\dot{\boldsymbol{\alpha}}_k = C_k \frac{1}{\sigma^0}(\boldsymbol{\sigma} - \boldsymbol{\alpha}_k)\dot{\bar{\varepsilon}}^{pl} - \gamma_k \boldsymbol{\alpha}_k \dot{\bar{\varepsilon}}^{pl} \tag{2.8}$$

where C_k is the initial kinematic hardening modulus and γ_k determines the rate at which the kinematic hardening modulus decreases with increasing plastic deformation.

The isotropic hardening law is given by:

$$\sigma^0 = \sigma|_0 + Q_\infty(1 - e^{-b\bar{\varepsilon}^{pl}}) \tag{2.9}$$

where $\sigma|_0$ is the yield stress at zero plastic strain, Q_∞ is the maximum change in the size of the yield surface, and b defines the rate at which the size of the yield surface changes as plastic straining develops.

The values for the variables required in the previous hardening laws are taken from Ringsberg, et al. [8] and correspond to a pearlitic rail steel. Characterizations of the cyclic behavior of railway-wheel-specific materials are very limited and/or have not been sufficiently detailed for their analytical application in the Chaboche plasticity model with combined isotropic and kinematic hardening. On the other hand, the experimental determination of the wheel's material properties in terms of the utilized plasticity model was beyond the objectives of this study. Accordingly, the material properties and hardening parameters for pearlitic rail steel used in this study are given below:

- Modulus of elasticity, E = 209 GPa
- Poisson's ratio, $\nu = 0.29$
- Initial yield stress, $\sigma|_0 = 406$ MPa
- Initial kinematic hardening modulus, $C_k = 13.2$ GPa
- Kinematic hardening modulus decreasing rate, $\gamma_k = 3.12$
- Maximum change in the size of the yield surface, $Q_\infty = 152$ MPa, and
- Yield surface development rate, b = 3.97

The nonlinear definition of the material properties is supplemented by the consideration of geometrical nonlinearity in the analyses.

2.5.2 Finite Element Analysis of Wheel-Rail Contact

2.5.2.1 Wheel-Rail Finite Element Model

The programs used for modeling (preprocessing) and performing the required FE analyses (FEAs) are HyperMesh 13® [43] and Abaqus 6.13® [44], respectively. The FE model (Figure 2.7) consists of a single railroad wheel, a contributory portion of the axle that it is attached to, and a rail segment with profiles provided by the American Association of Railroads (AAR). The wheel has a diameter of 914 mm (36 in.) and it's modeled under different vertical load of 162 kN and 233 kN. This load corresponds to a realistic weight estimation that is amplified to account for dynamic effects. This force is applied at a point on the longitudinal axis of the axle that is located where the wagon is supported. The contributory length of the axle in the FE model corresponds to half its actual

length, which accounts for the symmetry of the actual wheel-axle assembly. The rail segment has a length of 600 mm, which is a typical practical distance between ties/sleepers.

In the FEM snapshot given in Figure 2.8, the portion of the mesh denoted in white is subjected to the following boundary conditions. Due to symmetry, the displacements along the longitudinal axis of the axle are restrained at the end of the contributory axle corresponding to the middle of the actual axle; the rail is restrained at its ends on its longitudinal axis to also account for symmetry and continuity with the rest of the "infinite" rail. Portions of the bottom of the rail are fixed at the locations where the rail segment is assumed to make contact with the ties. Although, in reality, this latter is a contact boundary condition fixing the nodes is justified because the effects of the fixities of these nodes on the stress response of the wheel are minimal.

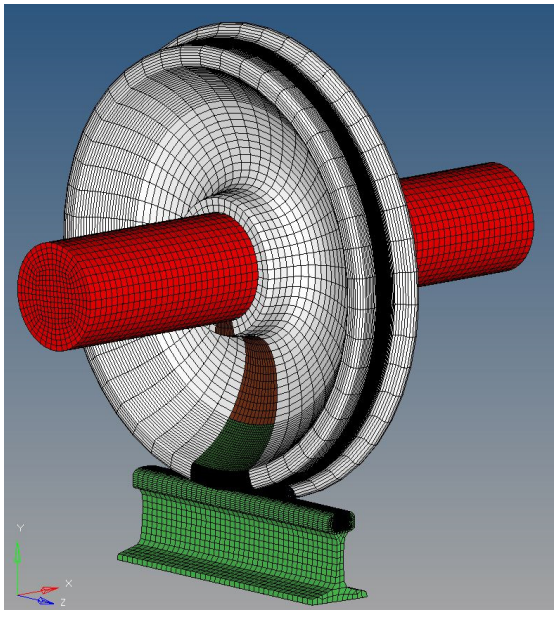

Figure 2.7. Finite element model of the wheel and rail

The type of element used in the mesh is an 8-noded reduced-integration solid (ABAQUS C3D8R element-type); that is, linear interpolation is used between nodal values for the primary variables as well as for the geometry. The selection of an element with linear interpolation was made because second-order elements can cause problems when hard contact between elements is enforced (as it is in this study) because of the way consistent nodal pressure loads are calculated. For instance, the equivalent nodal pressure forces for a three-dimensional, second-order brick element do not have the same sign for the case of a constant pressure, which makes it difficult for the hard-contact numerical algorithm to work correctly, especially for the case of non-uniform contact [44]. On the other hand, equivalent nodal forces in first-order elements always have consistent sign and magnitude; therefore, there is no ambiguity about the contact state that a given distribution of nodal forces represents.

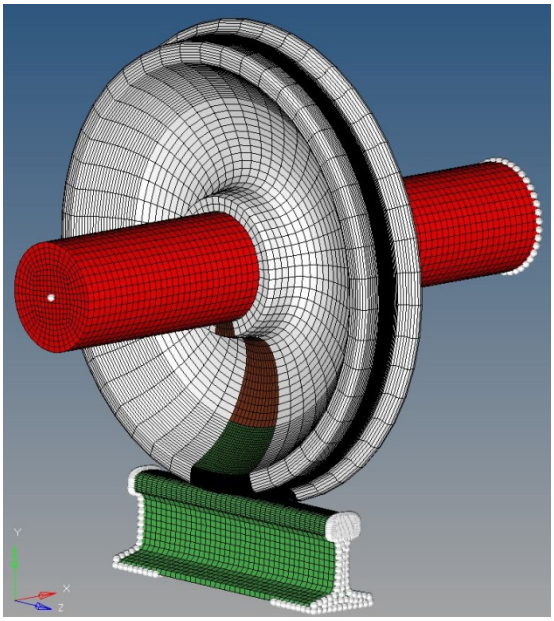

Figure 2.8. Finite element model: boundary conditions

For accuracy, precision, resolution, and numerical efficiency, the FE mesh in the wheel's and rail's regions in the vicinity of the contact areas were greatly refined.

Figure 2.9 and 2.10 illustrate the level of mesh refinements performed in the regions adjacent to the areas that are expected to make contact. The element size in the refinement area is about 1.3 mm wide × 1.4 mm deep × 2 mm long in the wheel and rail. The yellow color mesh in the wheel is the fatigue fracture plane that is studied in section 3 to find the critical plane. The x and y shown in future plots are based on their definition in Figure 2.9.

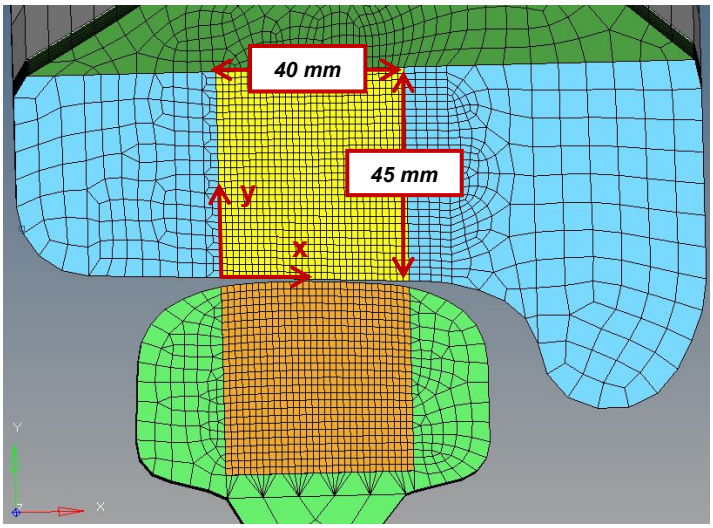

Figure 2.9. Finite element mesh: wheel/rail mesh in the region of contact. The yellow 40x45 mm^2 box is the studied cross section (fatigue fracture plane depicted in Figure 2.5)

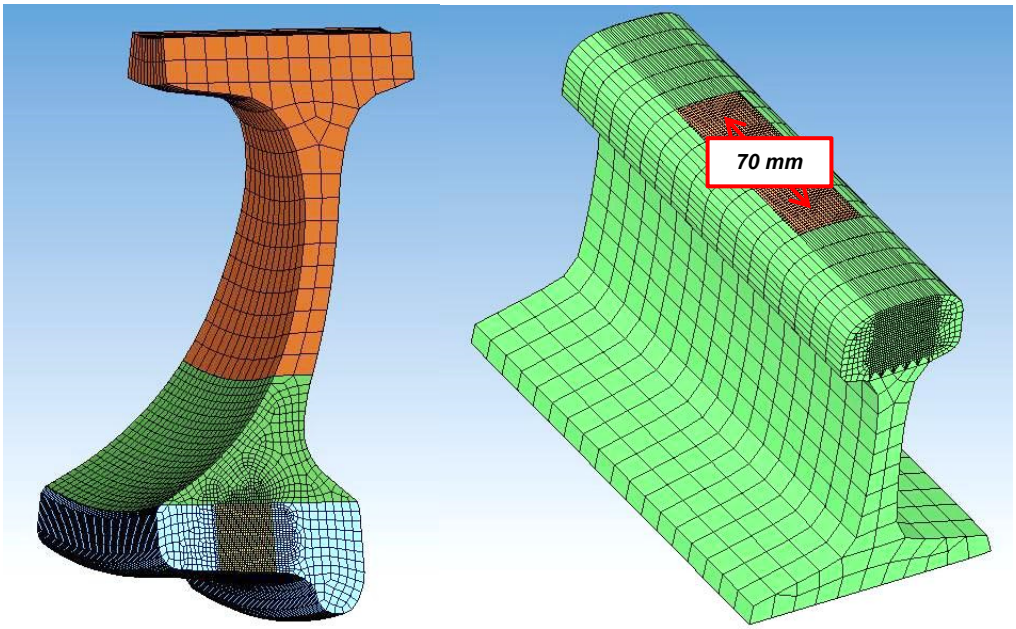

Figure 2.10. Finite element mesh: mesh refinement in the region of contact. Rolling trajectory is illustrated on the rail

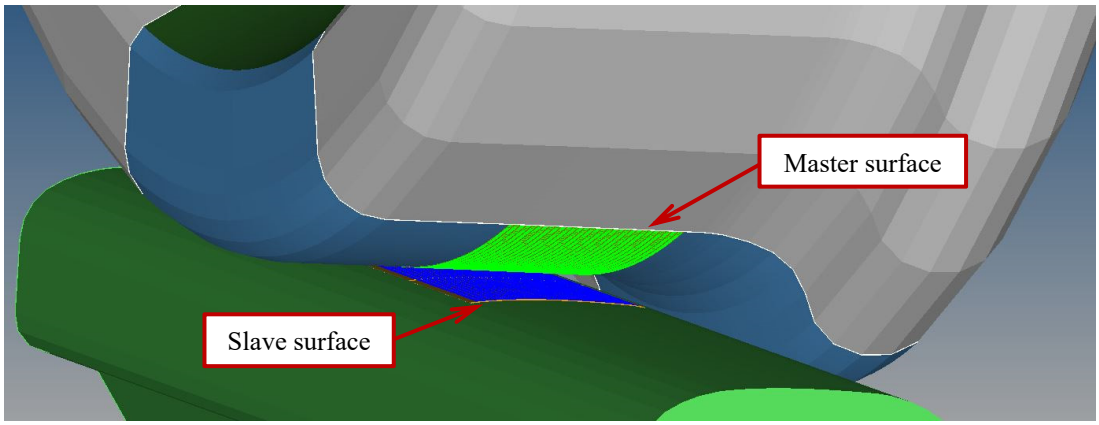

Figure 2.11. Wheel/rail master/slave contact interface

Contact algorithm used in this study is the Lagrange multiplier method with hard contact to avoid errors from excessive penetrations between nodes in contact. The contact pressure over-closure relationship used for the elements in contact is of the “hard” type. This type of relationship minimizes the penetrations along the defined contact sur-

faces and does not allow the transfer of tensile stresses across the contact interface, which is how the rail-wheel contact takes place in reality. The contact in wheel-rail interface is the element-to-element type with a strict master-slave relationship and the finite sliding algorithm. Surfaces of the wheel and rail expected to make contact are defined as a master and a slave surface respectively, as shown in Figure 2.11. The element size around the areas of contact was, in part, selected in consideration of this master-slave relationship. Only in the rolling step, a friction coefficient of 0.3 is applied to the contact definition to nucleate rolling action of wheel in driven condition as a result of the translation of the axle-wheel unit in longitudinal direction as shown in Figure 2.12. The applied friction coefficient has been commonly employed in steel-to-steel rolling-contact analytical studies [25].

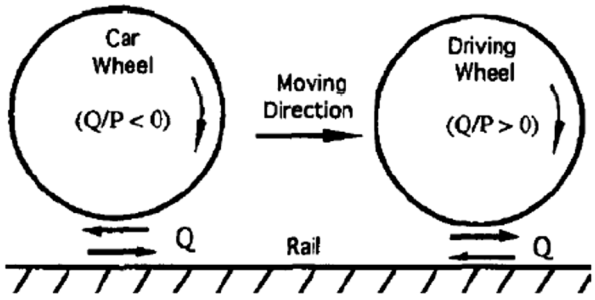

Figure 2.12. A schematic shows the driven wheel (left) and driving wheel (right) [45]

For computational efficiency, only elements near the region expected to make contact, i.e. the elements located around 0 – 45 mm from running surface of the inner part of the wheel/rail (0.5 degree-per-element of the wheel), are defined with the nonlinear isotropic/kinematic hardening material behavior (illustrated in yellow blocks in Fig-

ure 2.13). The elastic material behavior is used in the rest of the model (white transparent area in Figure 2.13). Due to symmetry, half of the axle-wheel unit is modeled with a symmetric boundary condition at the mid-length of the axle by preventing the lateral displacement of the axle-wheel unit. Varied amount of wheel loads is imposed on a node of the axle on field-side through a mass element with gravity, so that a resultant force due to wheel load remain in the vertical direction as wheel rotates. At both ends of the rail model, the end cross sections are prevented from moving in the longitudinal direction, and the nodes at the rail base, located at 0–10 mm from both rail ends, are prevented from moving in the vertical direction as they are supported by ties. This will allow the effects from global bending to be included in the rolling contact.

In summary, the axle-wheel model has approximately 241000 elements, and the rail model has approximately 82000 elements.

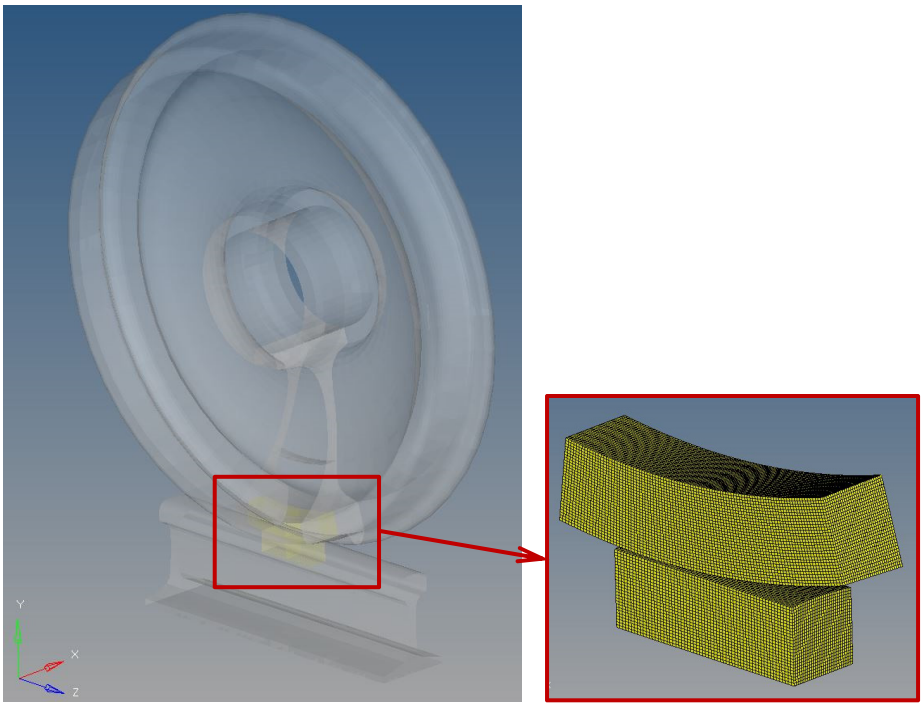

Figure 2.13. Transparent areas defined with elastic material behavior and the two yellow blocks defined with the nonlinear isotropic/kinematic hardening material behavior

2.5.2.2 Loading Steps to Simulate Rolling-Contact

The simulation of the actual rolling of railway wheels is performed by sliding the FE rail model to induce the rolling motion to the wheel in a distance of 70 mm in 1-mm increments. A previously carried-out FE study on the RCF of rails that uses the same wheel and rail profiles [39] determined that this rolling distance was sufficient to capture the "full" stress/strain response that takes place during rolling at any component cross-section. Therefore, in this study the evaluation of the stress/strain response and fatigue life of the modeled wheel is performed at a cross-section located in the middle of the rolling trajectory of the wheel; that is, the wheel cross section that is most directly in contact with the rail once the wheel has been rolled a distance of 35 mm. The model is

analyzed with two different material properties to compare and investigate their behavior; first with elastic material and then with hardening material. All simulations are performed as the following:

- Applying a vertical displacement to initiate a firm wheel/rail contact,
- Initiating rolling contact (stress /strain fields recorded in this step are used in fatigue damage analysis in next section),
- Moving the wheel up to eliminate contact (Residual stresses/strains are recorded at the end of this step),
- Repeating the cycles until residual stresses reach the steady-state.

2.6 Results and Discussion

A typical wheel load of 162 kN is assumed as a benchmark to investigate the change of various parameters, e.g. amount of wheel loads and mechanical behavior of the wheel steel on rolling stresses/trains as well as development of residual stresses at the wheel's subsurface level. Three principal axes of interest in the wheel model are the vertical, longitudinal, and transverse axes as illustrated in Figure 2.14. The normal stress directions are defined according to these three principal axes. The cross section of interest (fatigue fracture plane) is located at the middle — 35 mm from the starting point — of the 70 mm-long rolling path, right under the point of contact as shown in Figure 2.10. In this study this area will be investigated unless specified otherwise. Results will be reported for the rectangular cross-section at center or sometimes only for the vertical line of nodes right under the wheel-rail contact, as shown in Figure 2.15, as appropriate.

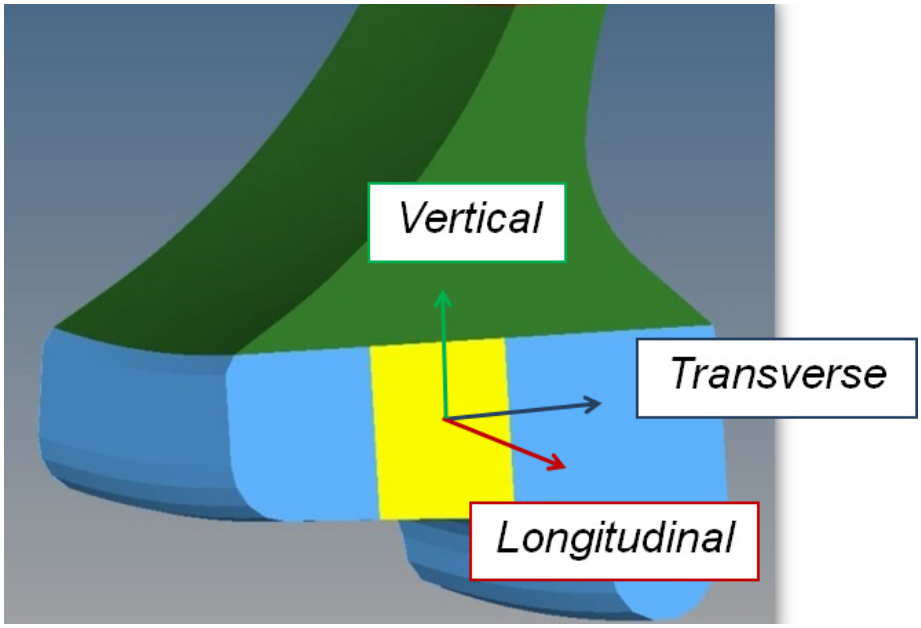

Figure 2.14. Principal axes of interest in the wheel model

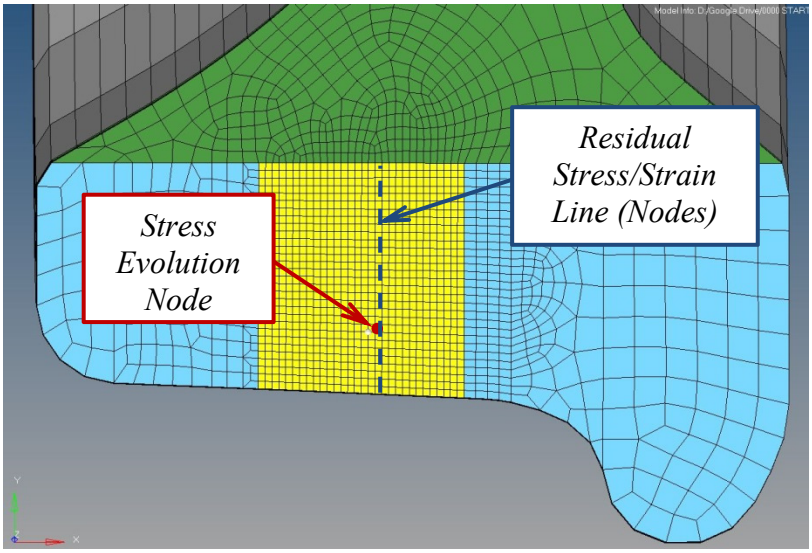

Figure 2.15. Locations of stress evaluation node and residual stress/strain line

2.6.1 The Steady State of Residual Stresses

The inelastic nature of materials, and particularly that of steel, produces residual stresses and strains as a byproduct of their cyclic response. As wheels roll on a rail, the yield surfaces of the material indicate that they expand and translate until they reach a final (steady-state) configuration. This is not only a result of the material model that is used, but the representation of what happens in reality when plastic materials respond in their inelastic range.

The predicted steady state stress/strain response is reached quickly; therefore, railway wheels and rails respond steadily during virtually their whole service life. This is why any study involving rolling contact between wheels and rails needs to be performed based on stabilized material conditions. If stresses and strains corresponding to the very first cycle(s) were used, different fatigue-life predictions would be obtained depending on the cycle chosen for the application of the fatigue model. These would most likely be in disagreement with field and experimental tests. To reach the steady state of stress/strain response in the constructed FE model, the wheel is "rolled" several times on the rail until analytical evidence exists that the stress-strain response of the material has been stabilized (within an acceptable range). A plot of the residual-stress progression at a node located approximately 15 mm below the running surface (see Figure 2.15) of the wheel is given in Figure 2.16.

Figure 2.16 shows that the residual stresses in the wheel are essentially stabilized after the fifth cycle, which agrees with the findings of Kabo and Ekberg [46] (Figure 2.17). Because of the periodic nature of the contact loads between the wheel and rail,

this at-the-end-of-cycle stabilization indicates a reached state of either elastic or plastic shakedown. In any case, stress/strain time-histories obtained from any cycle after the fifth one can be used for the fatigue analysis of the wheel. In this study, those resulting from the sixth loading cycle are used in the prediction of the fatigue related results.

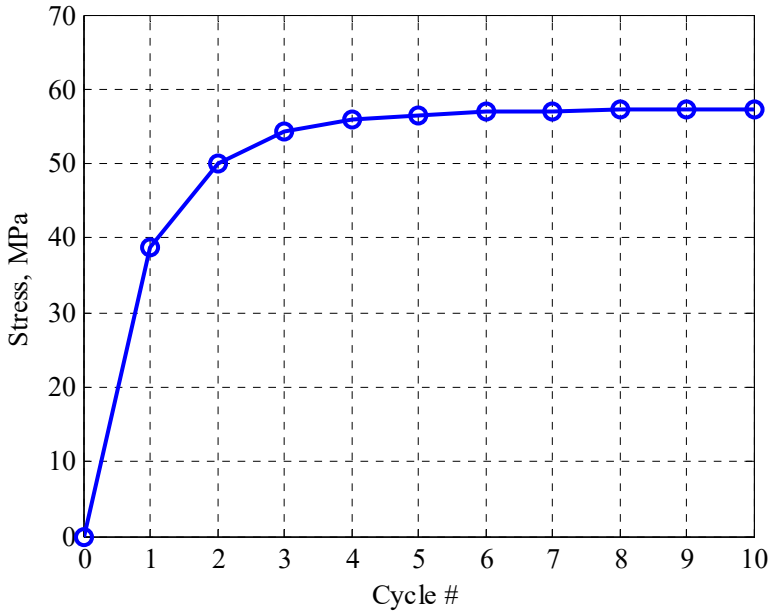

Figure 2.16. Predicted cyclic residual stress evolution in the wheel

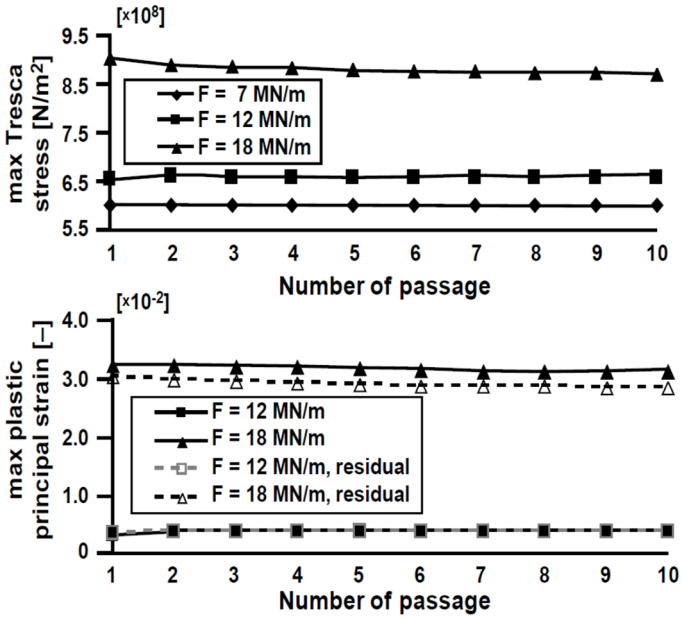

Figure 2.17. Material response stabilization in a planar FE model with Hertzian contact [46]

2.6.2 Accumulation of Residual Stresses in Rolling Contact

Residual stress results are recorded for all nodes vertically located exactly beneath the point of contact from depth of 0 to 45 mm (see Figure 2.15). Figure 2.18 and Figure 2.19 show residual stress profiles accumulated along those nodes at the end of sixth loading cycle with the 162 kN and 233 kN wheel loads, respectively. In these plots, 'y = 0' represents the wheel's running surface level (wheel tread). It shows that, at all depths, the accumulation of residual shear stresses is much less significant when compared to those of residual normal stresses. This justifies the use of the normal component of residual stresses for finding the number of cycles to their steady-state which agrees with Tangtragulwong [39] findings about the railhead.

Following discussion is based on the 162 kN and 233kN wheel loads residual stress analyses (Figure 2.18 and 2.19). At the near running surface (from 0-15 mm beneath the wheel tread), there are compressive residual stresses in all three directions as a result of severe plastic deformation from concentrated load. The transverse (σ_x) and longitudinal (σ_z) residual stresses reach their maximum of approximately -250 MPa at 5 mm. Profiles of the recorded residual stresses from the constructed FE model of the wheel are in agreement to the measured results from previous research (see [47], [48], and [49]).

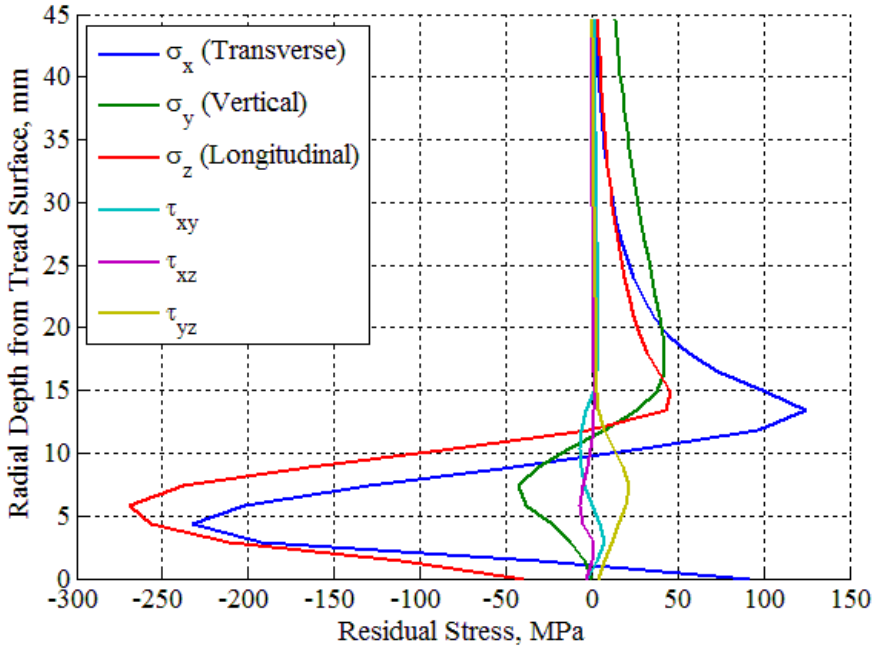

Figure 2.18. Predicted residual stress distribution after the sixth load-cycle along a line in the wheel's cross-section of interest (wheel load 162 kN)

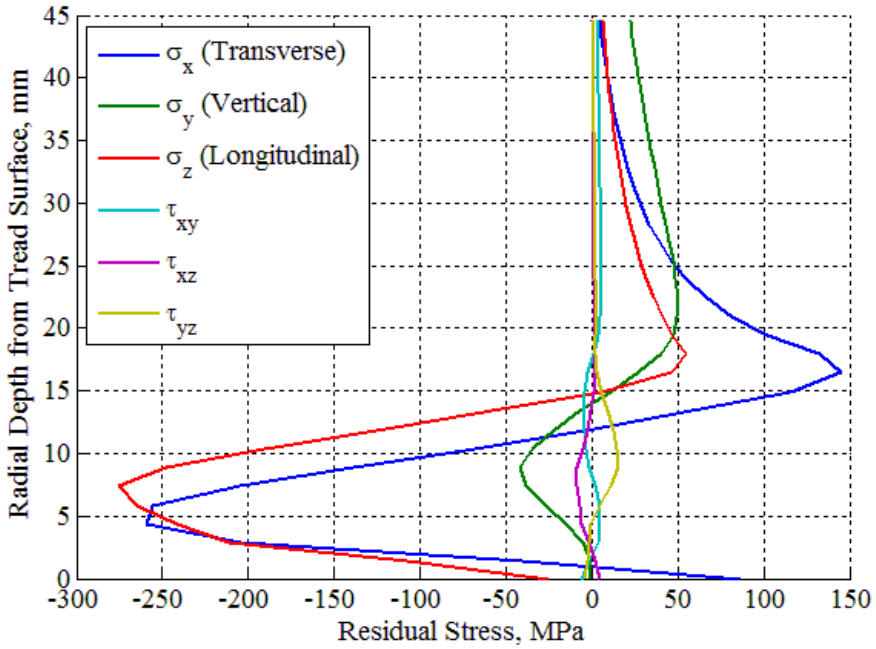

Figure 2.19. Predicted residual stress distribution after the sixth load-cycle along a line in the wheel's cross-section of interest (wheel load 233 kN)

2.6.3 Comparisons between the Equivalent Rolling Stresses of Elastic and Hardening Materials

Figure 2.20 shows the comparison of von-Mises stress contours at the wheel subsurface (the yellow colored area illustrated in Figure 2.9) between the analyses with an elastic material and a hardening material at sixth loading cycle.

For elastic material the equivalent rolling stress is localized about 4 mm beneath the wheel's tread with a maximum value of 931 MPa. This maximum value gradually decreases to around 100 MPa at 30 mm.

With Chaboche plasticity model, the peak equivalent stress is observed at greater areas (less stress concentration) located at surface and subsurface of the wheel with smaller magnitude of 453 MPa. The material in those areas strain hardened due to plastic deformation during the revolutions of the wheel on the rail until residual stresses reach the steady state at sixth cycle. Tangtragulwong [39] reported the same behavior in rail-heads.

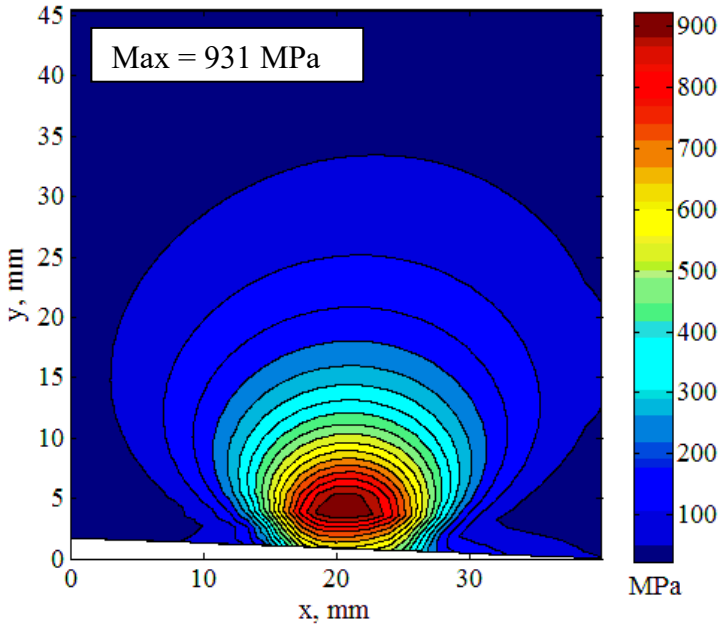

(a)

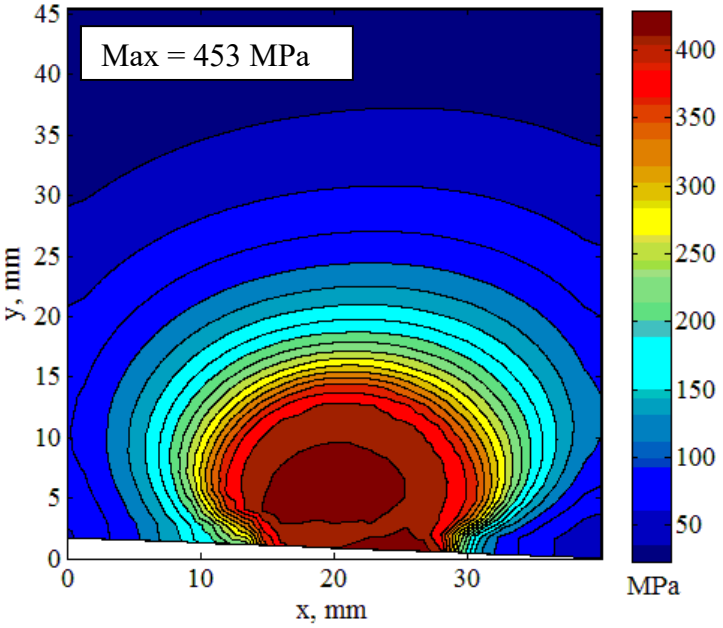

(b)

Figure 2.20. von-Mises contact-stress response at the wheel's cross-section (shown in different scales) for: (a) elastic material, and (b) hardening material at sixth cycle

2.6.4 Comparisons between the Rolling Stresses of Elastic and Hardening Materials

Figure 2.21, 2.22, 2.23, and 2.18 show comparisons of rolling stresses (normal and shear components) between the elastic and hardening cases at four different depths from wheel's tread. Following is the discussion regarding the influence of depth in the two material cases.

For elastic case, profiles of rolling stresses at different depths are similar with different magnitudes. Large normal stress (S_{yy}) and reversal shear stress (S_{yz}) are found in all levels of depths as predicted by analytical solution from the Hertzian contact theory (Johnson [21]). The longitudinal stress (S_{zz}) is compressive near wheel tread. It gradually diminishes and eventually turns to tensile stress at 40 mm. The transverse stress (S_{xx}) is compressive near wheel tread. It then turns to be tensile at greater depth with relatively small magnitude. Considering that the normal stresses are mostly compressive in the elastic material case, the chance of fatigue crack nucleation which is encouraged by mean tensile stresses is relatively low.

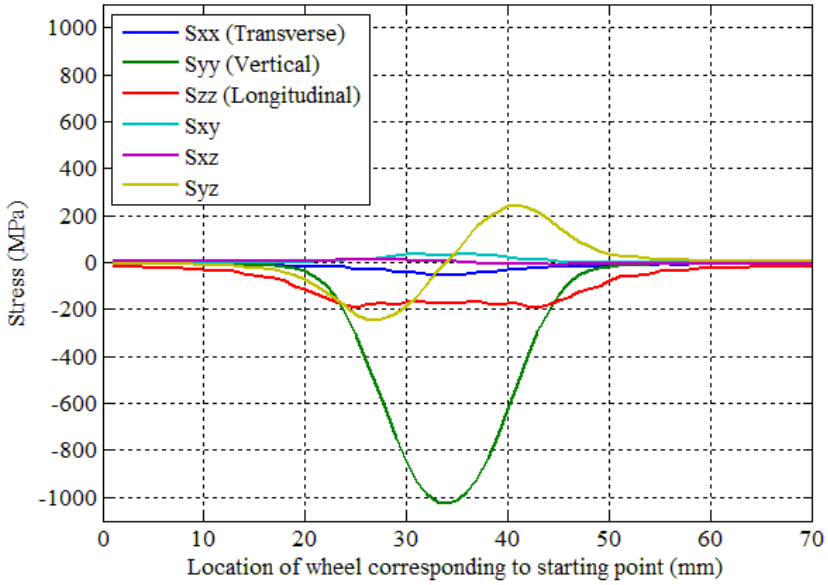

(a)

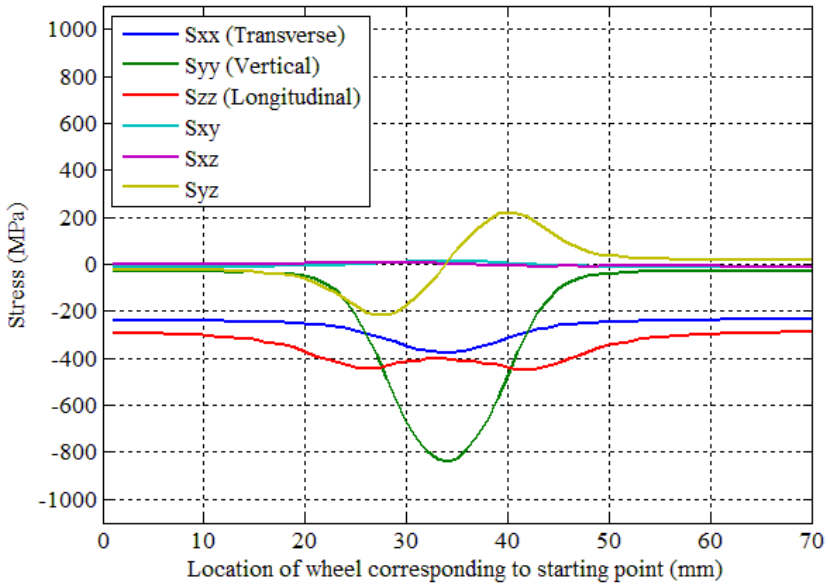

(b)

Figure 2.21. Rolling stresses of a node located at 5 mm below running surface for: (a) elastic material, and (b) hardening material

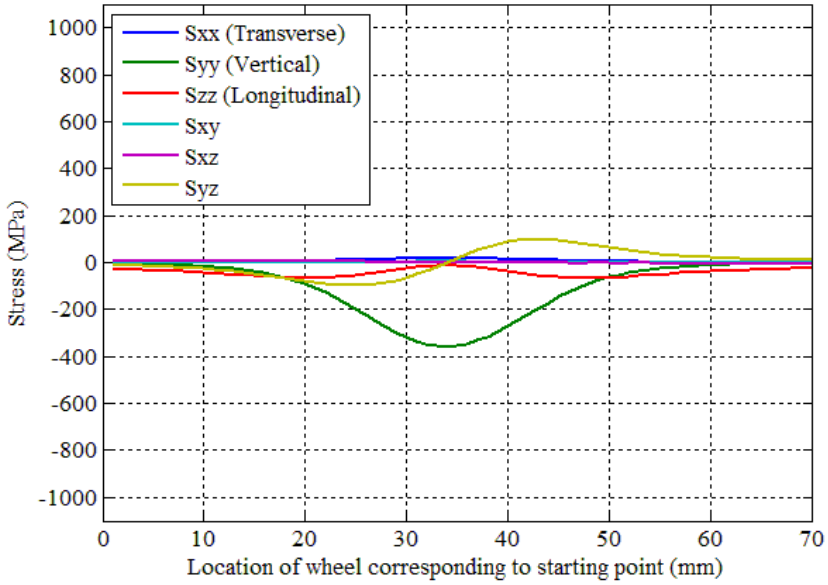

(a)

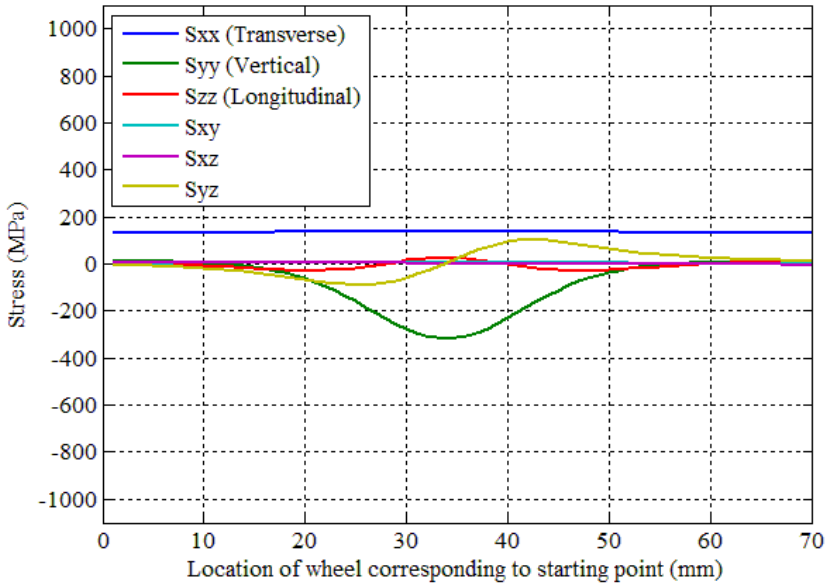

(b)

Figure 2.22. Rolling stresses of a node located at 13 mm below running surface for: (a) elastic material, and (b) hardening material

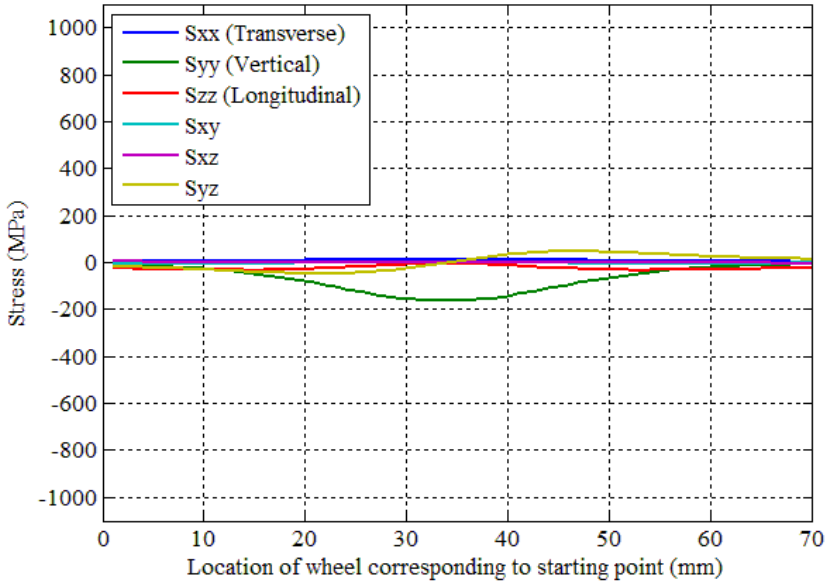

(a)

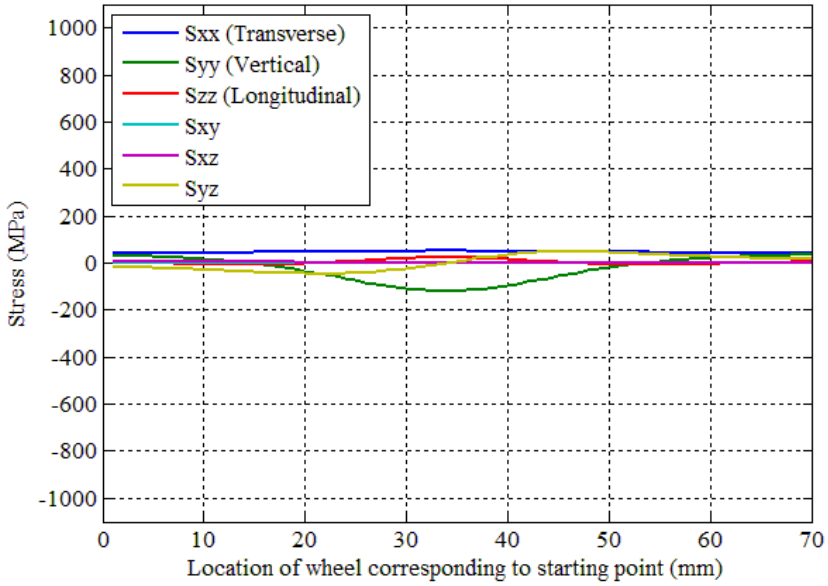

(b)

Figure 2.23. Rolling stresses of a node located at 20 mm below running surface for: (a) elastic material, and (b) hardening material

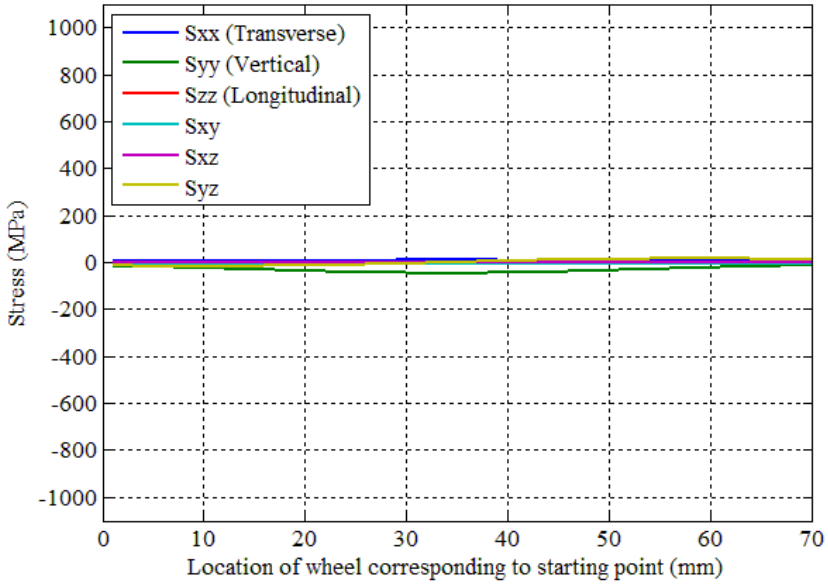

(a)

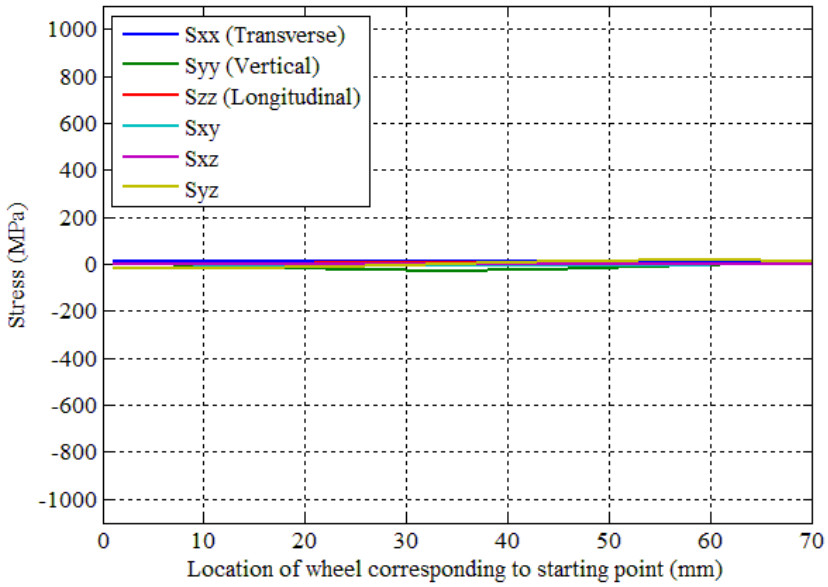

(b)

Figure 2.24. Rolling stresses of a node located at 40 mm below running surface for: (a) elastic material, and (b) hardening material

Following observations from hardening material case can be drawn based on the comparison with elastic material case:

1. At 5 mm below the wheel tread, the longitudinal (S_{zz}) and transverse (S_{xx}) stresses are compressive with higher value than elastic material case due to strain hardening and the compressive residual stresses.
2. At 13 mm below the wheel tread, the longitudinal (S_{zz}) stress changes from compression to tension and the transverse (S_{xx}) stress is tensile during the wheel/rail rolling.
3. At 20 mm below the wheel tread, the stress profiles are like the 13 mm depth but with considerably lower magnitudes.
4. At 40 mm below the wheel tread, no significant changes of rolling stresses observed.
5. The shear stress changes are mostly significant at near tread area (5 mm level).

2.6.5 Accumulation of Residual Strains in Rolling Contact

As it's mentioned in section 2.5.1, ratchetting is also considered as one of the damage modes in rolling contact. Ratchetting is defined as a continuous accumulation of strain in the direction of applied mean stress. As ratcheting progresses, it exhausts the ductility of material, leading to failure of structure when total strain accumulation reaches critical limit [39].

Figure 2.25 shows the residual strains at the end of the sixth loading cycle for the 162 kN wheel load. The data is for the nodes vertically located right beneath the point of

contact from depth of 0 to 45 mm (the node line is shown in Figure 2.15). Three strain components of ε_x ,ε_y , and γ_{yz} show significant accumulation of residual strains at 10 mm below wheel tread. The deformation in vertical direction is due to compression and in transverse direction is lateral and longitudinal due to the Poission's effect. Additionally by comparing Figure 2.25 with Figure 2.26, it can be concluded that the magnitude of the strain is proportional to the wheel load. Constrained by boundary conditions at longitudinal direction, deformation in this direction is limited (low ε_z). In contrast, wheel rim is not restrained in lateral direction; therefore, larger material deformation is observed in the form of transverse residual strain accumulation.

The negative shear strain in vertical plane of yz implies forward flow of material at subsurface level of wheel rim meaning the material flow in the rolling direction. Tangtragulwong [39] explained the same phenomenon happening near running surface of the railhead which qualitatively agrees with experiment results by Shima, et al. [50] and Hamilton [51].

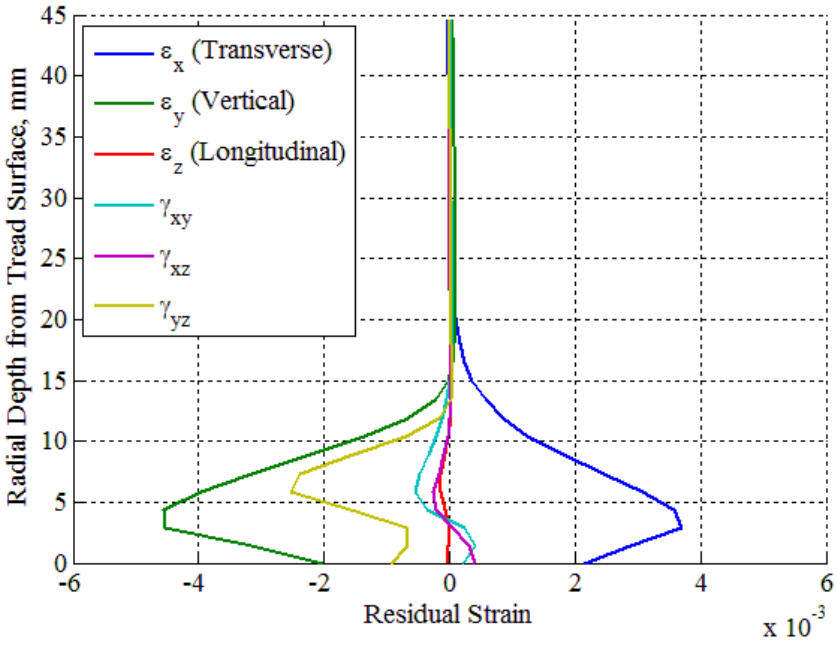

Figure 2.25. Predicted residual strain distribution after the sixth load-cycle along a line in the wheel's cross-section of interest (wheel load 162 kN)

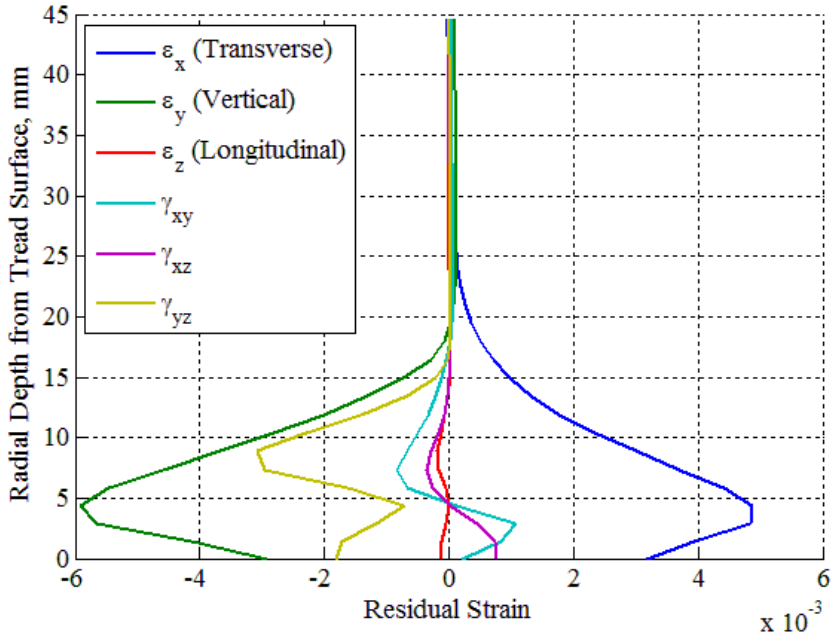

Figure 2.26. Predicted residual strain distribution after the sixth load-cycle along a line in the wheel's cross-section of interest (wheel load 233 kN)

2.7 Summary

- Residual stress reaches the steady-state after fifth loading cycle, showing that the normal components are compressive at closer to tread surface area (less than 15 mm depending on wheel axle load) while they are tensile at deeper region below running surface. The accumulation of the residual shear stresses is relatively small.
- While the maximum normal residual stresses are almost the same in both load cases, the change in the sign of the residual stresses (compressive to tensile) occur at approximately 3 mm deeper region for the 233 kN wheel load case as oppose to the 162 kN wheel load.
- Using Chaboche plasticity model, the peak equivalent stress (von-Mises stress) is observed at greater areas (less stress concentration) located at surface and subsurface of the wheel with smaller magnitude of 453 MPa. The material in those areas strain hardened due to plastic deformation during the revolutions of the wheel on the rail until residual stresses reach the steady state at sixth cycle. Same behavior observed in railheads in other studies.
- Profiles of the residual stresses predicted by the Chaboche plasticity model agree well with those from the measurement in literatures; however, to achieve more accurate results, equivalent field tests in accordance with the developed analytical procedure are necessary to calibrate the FE model herein.
- Wheel subsurface rolling stress history at the depth of 5 mm shows lower vertical stress for hardening material case compare to the totally elastic material case whereas the transverse and longitudinal stresses are relatively larger in harden-

ing material case. At deeper subsurface level of 13 mm, the only difference between two material cases observed was the tensile transverse stress history in hardening material case which can be in favor of fatigue cracks formation and growth.

- The magnitude of the strain accumulation – and possible subsequent ratchetting of material – is proportional to the wheel load; the more wheel load, the higher strain accumulation is recorded.
- The negative shear strain in vertical plane of yz implies forward flow of material at subsurface level of wheel rim meaning the material flow in the rolling direction. The same phenomenon is reported near running surface of the railhead.

3 FATIGUE DAMAGE ANALYSIS OF A 'DEFECT-FREE' WHEEL

3.1 Introduction

This section is concerned with the implementation of a strain-based critical-plane criterion to estimate the fatigue-initiation life of the railway wheel FE model. For this purpose, the sixth loading cycle of the stress/strain response time-history obtained from the FE model is imported into MatLab® wherein the Fatemi-Socie fatigue criterion was implemented. This is a multiaxial strain-based critical plane criterion that can account for plastic behavior, and can therefore be applied to the HCF and LCF regimes [39].

3.2 Background

The RCF problem in railway wheels is not new; several studies have been made to predict the appearance of fatigue cracks in 'defect-free' materials. Many of them, in fact, follow the same philosophy of the investigation in this study; however, as said before, practically all of them make use of a form of analytical simplification and/or do not include all the factors influencing fatigue-crack initiation, i.e., they either use Hertzian contact, elastic material models, plane analytical models, or stress-life approaches. Some of these past research efforts are outlined in the following paragraphs.

One of the railway-wheel RCF studies was made by Lundén [52]. He investigated the combined effect of a periodically varying contact-pressure and an intermittent thermal brake loading on the contact-fatigue of railway wheels. He used Hertzian contact

in an axi-symmetric finite element (FE) model that incorporated a bi-linear elasto-plastic material model. To estimate the fatigue-life of the wheel, the strain accumulation was used in a low-cycle-fatigue (LCF) analysis. One of the findings was that the use of temperature-dependent material properties had little influence on the predicted results. However, the author recognized the need for 3-D calculations and more sophisticated material models in order to achieve more reliable results.

Later, Ekberg [20] used a semi-analytic procedure with elastic materials, Hertzian theory, stochastic application of loads and the Dang-Van criterion to predict crack-initiation in 'defect-free' materials. However, his results did not correlate well with field data. Although they list special dynamic behavior and material imperfections as possible sources for the lack of agreement, the use of pure elasticity, Hertzian-contact, and a stress-life fatigue criterion suggests that a more accurate prediction would have been possible with the use of more appropriate analytical techniques.

Around the same time, Kabo and Ekberg [46] evaluated fatigue-crack initiation criteria in a pearlitic rail steel under states of elastic shakedown, plastic shakedown, and ratcheting. They used a 2-D FE model that incorporated Hertzian-contact and an elasto-plastic (Chaboche) material model for the analysis of stress. The fatigue analysis was done with the Dang Van and the Smith-Watson-Topper [32] fatigue criteria. Their analytical results showed reasonable agreement with experiments in the prediction of the fatigue-crack-initiation planes.

Ringsberg [9] developed a semi-analytical approach for contact-stress calculation that implemented a 3-D FE model acted on by a Hertzian-type contact loading. The fa-

tigue analysis of the resulting stresses made use of the Jiang fatigue criterion [53], which assumes that plasticity is the major cause of fatigue-damage, and therefore resorts to the cyclic plastic properties of the material.

Another simplified study was carried out by Sraml, et al. [54]. They first used Hertzian theory to determine contact stresses and deployed them within a uniaxial fatigue model based on principal stresses/strains. In an attempt to achieve improved accuracy, Guo and Barkey [55] used a 2-D FE model for the analysis of stress, whose results were combined with the multiaxial fatigue model developed by Fatemi and Socie described below.

Bernasconi, et al. [56] made an assessment of subsurface RCF in railway wheels. The method applied the Dang Van criterion to contact-stress histories obtained through a numerical procedure that used an elastic material model. The use of elasticity was justified on the assumption of an existing state of elastic shakedown in the region of interest. To validate their assessment, they performed uniaxial tension–compression, reversed-torsion, and non-proportional loading tests on specimens extracted directly from railway wheels. Their results, however, did not achieve favorable agreement with their predictions, which was presumably due to existing inconsistencies between the Dang Van model considerations and the nature of the experimental tests that they performed.

A year later, Bernasconi, et al. [22] compared experimental results obtained with R7T steel, typical in railway wheels, with predictions made using the Dang Van criterion; however, they again did not achieve good correlations, especially when they considered high compressive stresses.

Jiang, et al. [30] performed combined axial-torsional fatigue tests on a structural steel to evaluate the effectiveness of the Fatemi–Socie fatigue criterion, the Jiang criterion, and a short-crack-growth-based criterion [57]. The results of the study showed that fatigue-life predictions made with the use of the three criteria correlated reasonably well with experimental observations; however, discrepancies were found between the predicted and observed crack-plane directions.

Dang Van, et al. [31], Kabo and Ekberg [6, 46, 58-60] have produced several valuable results for the assessment of RCF in railway wheels. They developed a set of expressions in the form of fatigue indices developed from Hertzian-contact expressions, the Dang Van criterion, and fracture mechanics that take care of subsurface fatigue and fatigue initiated at deep defects, respectively.

3.3 Fatigue Index Calculation

The philosophy of total-life methods is to estimate the resistance to fatigue crack nucleation based on nominally defect-free parts. A drawback to the total-life method is that the definition of failure is not clear [9]. These methods analyze the total fatigue life to failure (crack nucleation in this case) and they are divided into stress-based and strain-based approaches. The stress-based (stress-life) approach is characterized in terms of low cycle stress ranges that are designed against fatigue crack initiation (high-cycle fatigue failures). However at high load levels, in the low cycle fatigue (LCF) regime, the cyclic stress-strain response and the material behavior are best modeled under strain-

controlled condition (strain-life approach) [61]. The stresses in this approach are high enough to cause plastic deformations that govern fatigue failure (LCF failure).

A strain-based total-life approach is employed in the current study. The strain-life approach used along with FE analyses makes a powerful combination since any arbitrary geometry with any material and loading can be analyzed for fatigue as long as the stress/stress fields can be captured from FE analyses (no need for assuming crack size, location, and orientation).

This section is concerned with the implementation of a strain-based critical-plane criterion to estimate the fatigue-initiation life of the railway wheel of the FE model. For this purpose, the sixth loading cycle of the stress/strain response time-history obtained from the FE model is imported into MatLab® wherein the Fatemi-Socie fatigue criterion was coded as a computer algorithm. This is a multiaxial strain-based critical-plane criterion that can account for plastic behavior, and can therefore be applied to the HCF and LCF regimes [39].

The model employed herein, originally proposed by Fatemi and Socie [35], is represented by the following equation:

$$FS = \frac{\Delta\gamma_{\max}}{2}\left(1+\eta\frac{\sigma_{n,max}}{\sigma_y}\right) \tag{3.1}$$

where $\Delta\gamma_{\max}$ is the maximum shear strain range in a cycle, $\sigma_{n,\max}$ is the maximum normal stress in a cycle, η is the normal coefficient, which is an empirical material constant, and FS is the Fatemi-Socie fatigue index.

The basis of the Fatemi-Socie (FS) model [32] is that the irregular shapes of crack surfaces produce friction forces that oppose shear deformations along the crack's plane. This mechanism impedes crack-growth, thereby increasing the fatigue life of the material. Presence of normal tensile stresses reduces the friction forces acting on the crack faces. If this reduction in the friction forces takes place, the crack-tips must carry a greater fraction of the far-field shear forces, which is assumed to favor the growth of the crack (Figure 3.1).

The FS model accounts for the interaction between cyclic shear strain and normal stress at a particular material point on a particular plane during a cycle of load. The normal stress across a plane accounts for the influence of friction.

The coefficient term used to include the influence of normal stress on the FS fatigue criterion is called the normal coefficient (η) in this study. It is material-dependent, and, for pearlitic rail/wheel steel, it is determined by a regression analysis of a set of fatigue life data from previous studies. The value of normal coefficient for pearlitic rail steel is determined from a regression analysis between the FS fatigue index and fatigue life data from literatures (Figure 3.2).

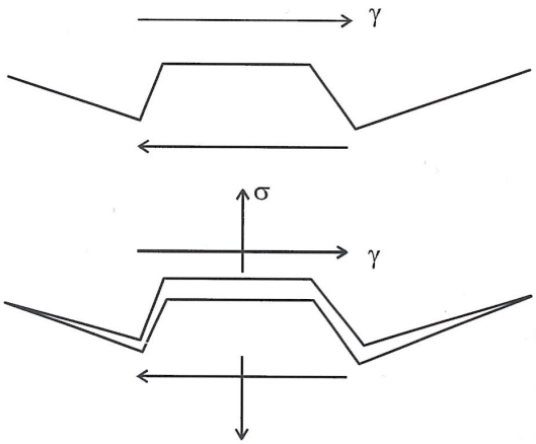

Figure 3.1. Physical basis of the Fatemi-Socie fatigue model [32]

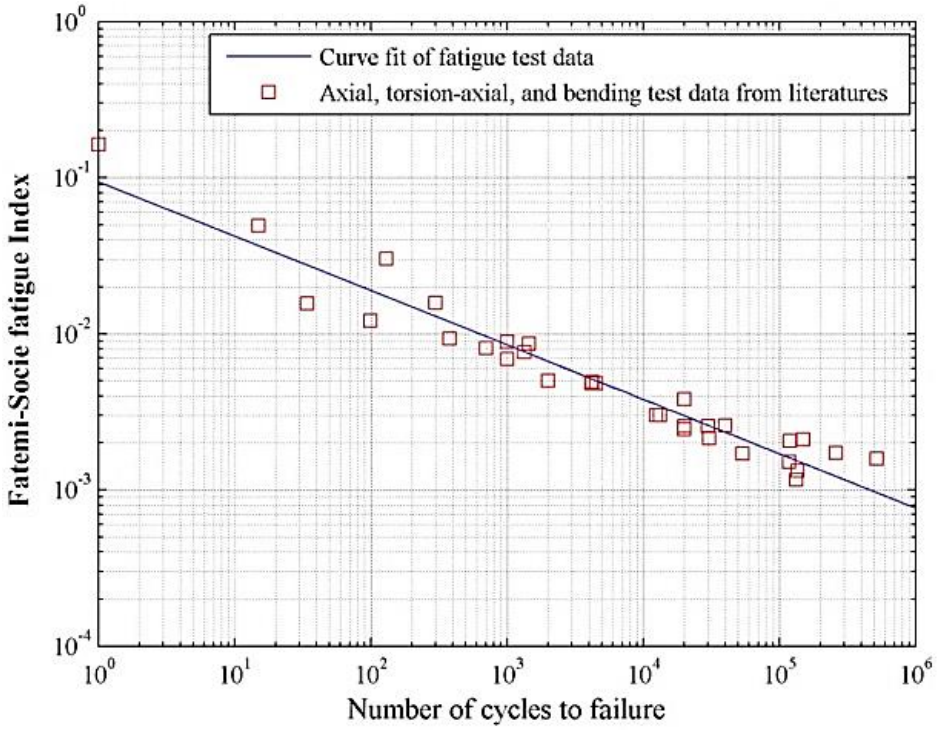

Figure 3.2. *FS* fatigue index correlation with the number of cycles to failure for a pearlitic rail steel ($\eta = 1$) [39]

In order to find the plane with the maximum FS fatigue index, an exhaustive search using the spherical coordinate throughout all possible planes is performed by varying the elevation (φ) and azimuth (θ) angles (Figure 3.3). However, to avoid excessive run time in both data processing and optimization steps, the plane search is performed with 10 degree increments of both φ and θ. The normal vector that defines a plane can be written as:

$$\overline{n} = \begin{Bmatrix} n_1 \\ n_2 \\ n_3 \end{Bmatrix} = \begin{Bmatrix} \sin\varphi\cos\theta \\ \sin\varphi\sin\theta \\ \cos\varphi \end{Bmatrix} \tag{3.2}$$

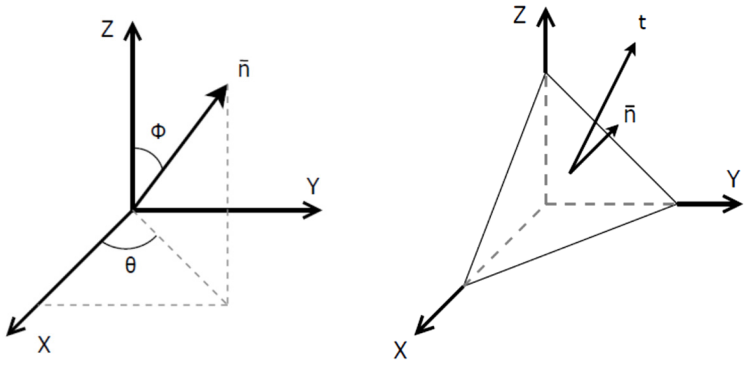

Figure 3.3. a) The spherical coordinate; b) Traction vector on each critical plane (Cauchy's law)

3.4 Results and Discussion

3.4.1 Fatigue Index of the 162 kN Wheel Load with Material Hardening

For each node in the yellow box of Figure 3.4, the *FS* fatigue index is calculated from a stress and strain tensor history for all selected planes. Among those planes, contours of the largest fatigue indeces for different normal coefficient (η) values are illustrated in Figure 3.5 to 3.7. The x and y axes are defined in Figure 3.4.

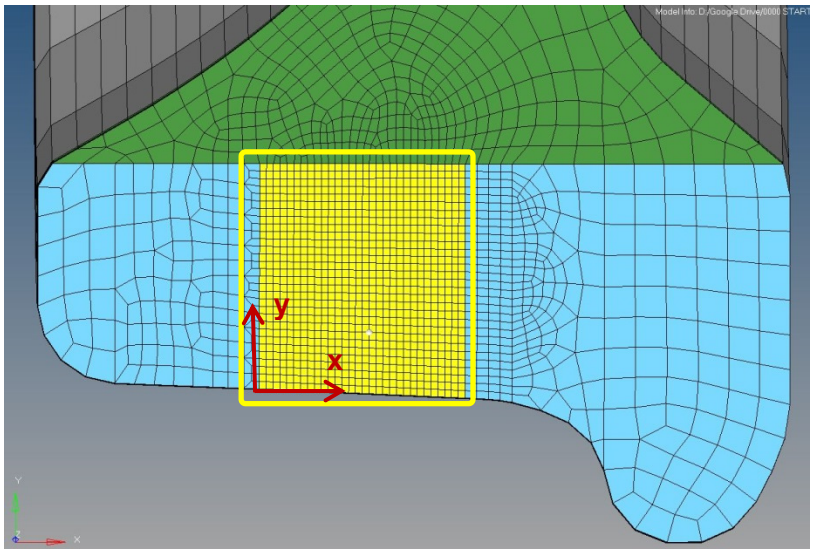

Figure 3.4. *FS* fatigue index region to study

Figure 3.5 illustrates the maximum FS fatigue damage index for $\eta = 0$, that is the crack nucleates solely by shear strain amplitude effect. The fatigue index is concentrated in an area 4-7 mm beneath the wheel tread with the maximum fatigue index of 0.0013755 at 3.7 mm depth. When $\eta = 0$ (participation of normal stress), the fatigue index is still around the same area, however with slightly lower peak value of 0.0013032

(Figure 3.6). The fatigue index contour for $\eta = 3$ shows less localized damage site as opposed to two previous cases with the lower pick value of 0.0012328 (Figure 3.7). Finally, for $\eta = 5$, Figure 3.8 shows multiple crack nucleation sites; at the surface and at a deeper depth of approximately 10 mm below running surface. It should be noted that the tensile residual stresses from rolling contact presented in section 2 are larger at the same area of 4-7 mm beneath the wheel tread. This could imply the importance of normal stress on residual stress accumulation as well as subsurface fatigue crack nucleation.

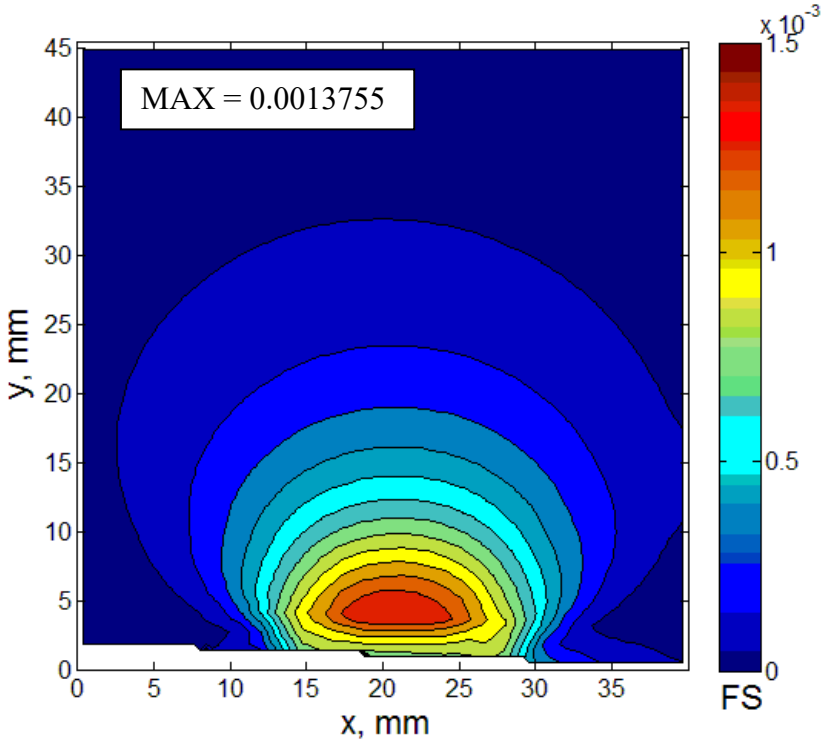

Figure 3.5. Maximum Fatemi-Socie fatigue index contour (η=0) of the 162 kN wheel load with hardening material at the sixth loading cycle by searching selected plane at all nodes

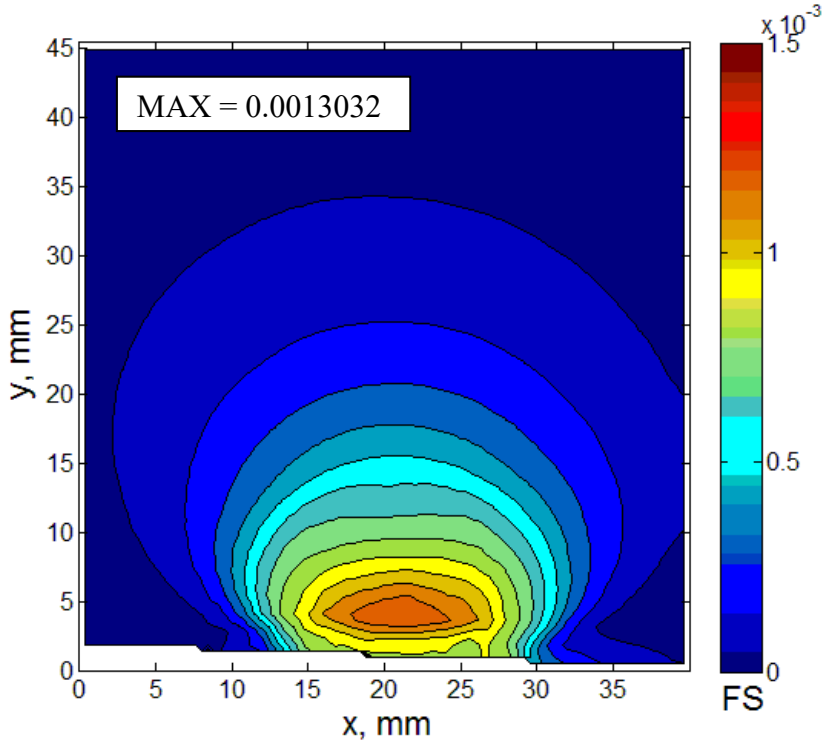

Figure 3.6. Maximum Fatemi-Socie fatigue index contour (η=1) of the 162 kN wheel load with hardening material at the sixth loading cycle by searching selected plane at all nodes

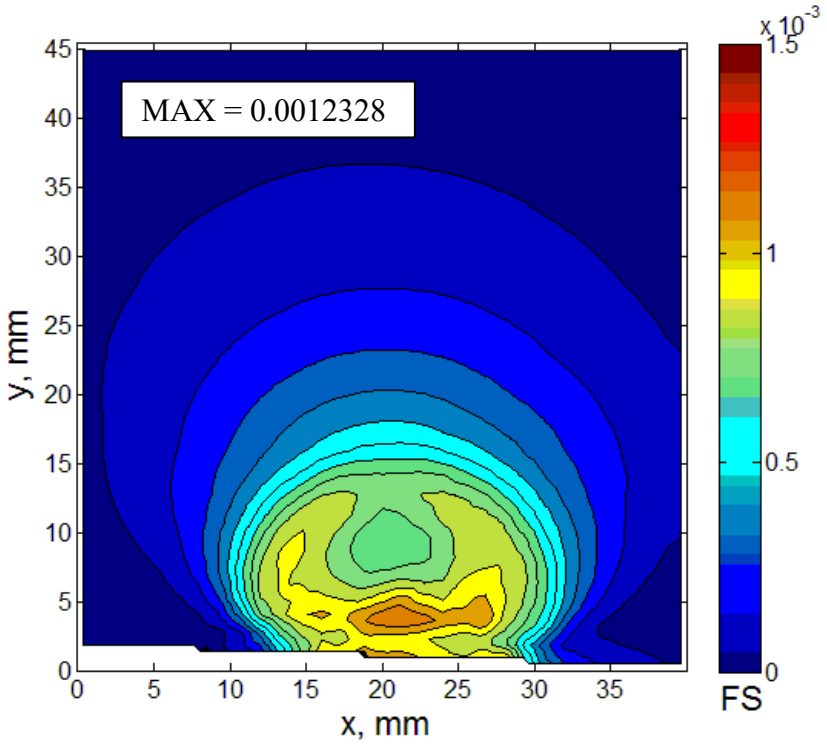

Figure 3.7. Maximum Fatemi-Socie fatigue index contour (η=3) of the 162 kN wheel load with hardening material at the sixth loading cycle by searching selected plane at all nodes

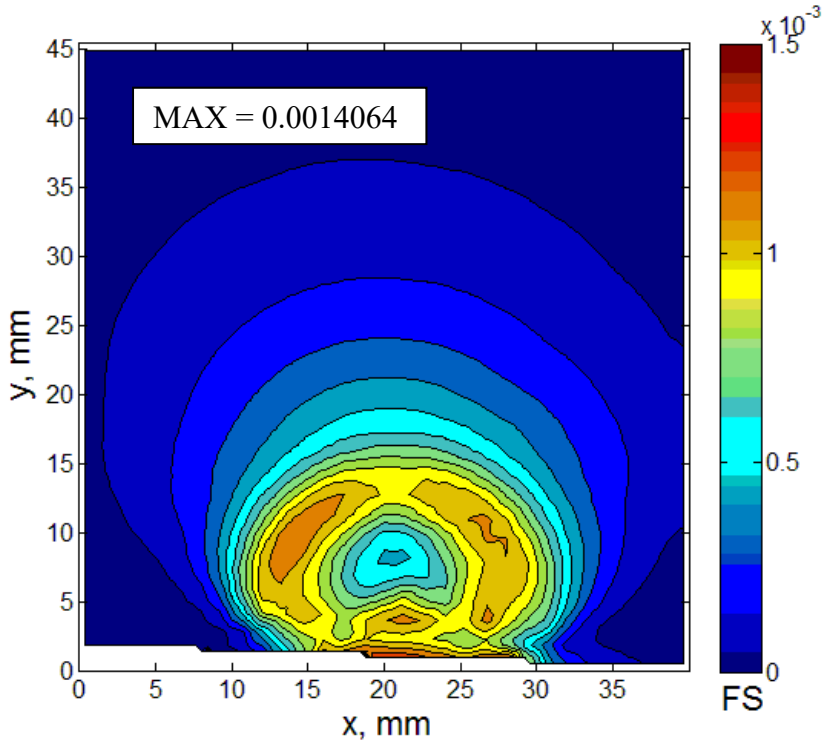

Figure 3.8. Maximum Fatemi-Socie fatigue index contour (η=5) of the 162 kN wheel load with hardening material at the sixth loading cycle by searching selected plane at all nodes

Table 3.1 summarizes the predicted crack depth and the approximated corresponding cracking plane for different normal coefficients. Defined in previous section, z-axis coincides with the longitudinal direction of a rail, while y-axis and x-axis coincide with the vertical and transverse directions respectively. For pearlitic rail/wheel steel (η=1), the value of y = 3.7 mm corresponds to a fatigue-crack initiation depth of about 3 mm, which is consistent with the findings of previous research [6]. The cracking plane is defined based on Figure 3.9 which for pearlitic rail/wheel steel, it's a mixed horizontal/vertical plane (more close to horizontal than vertical). Prediction of two near-surface fatigue crack nucleation sites in the case of η=3 and 5 as opposed to only one site in each case of η=0 and 1 shows the importance of the effect of the normal stress components.

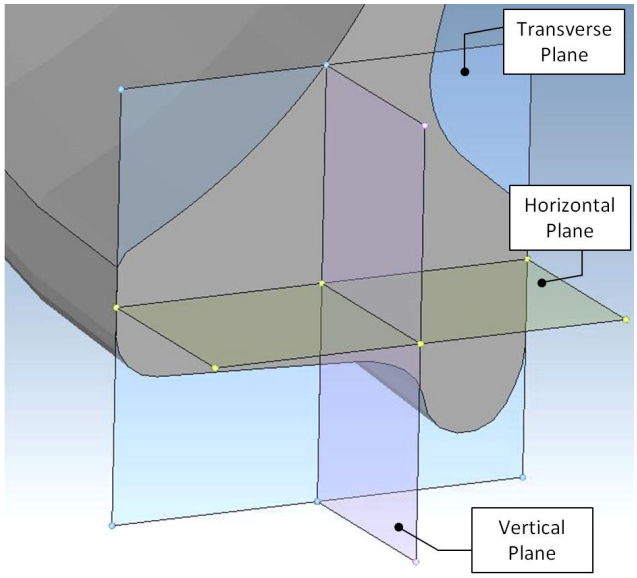

Figure 3.9. Planes of propagation for wheel subsurface crack.

Table 3.1. Summary of possible fatigue crack nucleation sites and cracking planes for the 162 kN wheel load with material hardening and different η values

Normal coefficient (η)	FS fatigue index	Depth below running surface (mm)	Unit normal vector of critical plane			Cracking plane
			x	y	z	
0	0.0013755	3.8	-0.72	-0.60	-0.34	Vertical/Horizontal
1	0.0013032	3.7	0.49	-0.85	0.17	Horizontal/Vertical
3	0.0012328	3.7	0.49	-0.85	0.17	Horizontal/Vertical
5	0.0014064	0.5	0.00	0.00	1.00	Transvers

3.4.2 Fatigue Index of the 162 kN Wheel Load with an Elastic Material

Implementing elastic material as an input in the FE model instead of hardening material results in higher and more localized fatigue indices in all cases (Figure 3.10 to 3.12). Fatigue index contours remain mainly unchanged as η increases from 0 to 5 with the maximum index of 0.0018257 for η=5 case. Comparing Figure 3.5 and Figure 3.10 (for the case of η=0), the fatigue index increases from 0.0013755 in hardening case (consideration of strain accumulation) to 0.0016832 by using elastic material. A similar behavior is observed in the simulation with η=1, 3 and 5 indicating the beneficial role of the strain accumulation on surface fatigue crack nucleation which contradicts the detrimental role of strain accumulation in failures due to ratcheting. This contradiction has also been observed in a similar study on rails by Tangtragulwong [39].

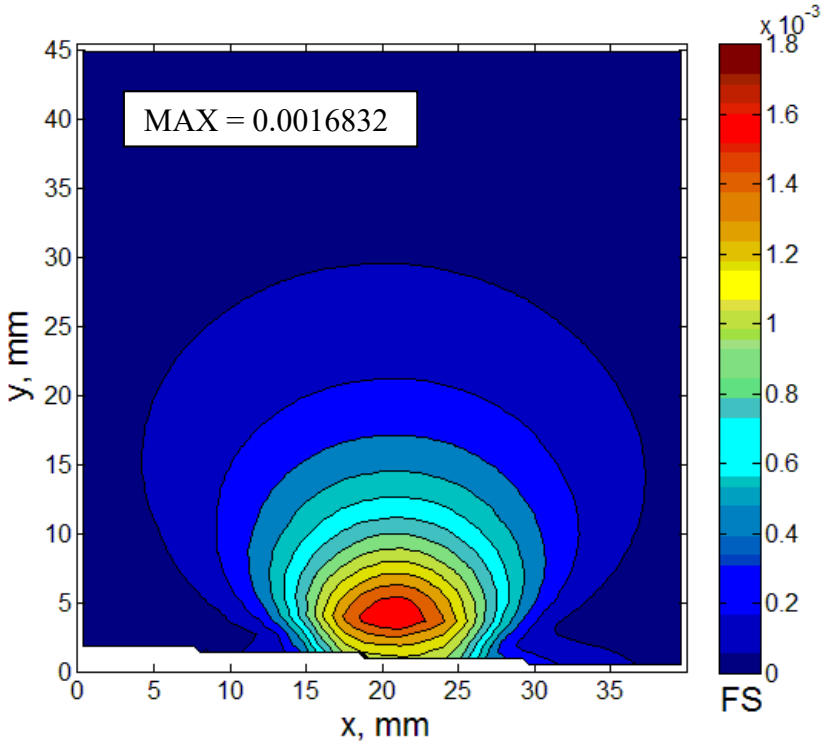

Figure 3.10. Maximum Fatemi-Socie fatigue index contour (η=0) of the 162 kN wheel load with elastic material at the sixth loading cycle by searching selected plane at all nodes

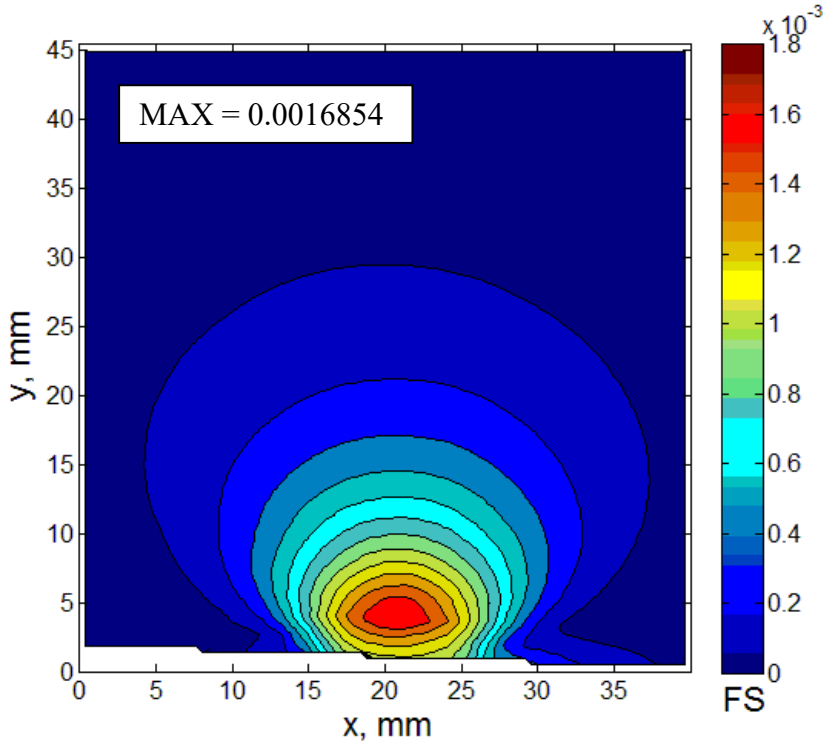

Figure 3.11. Maximum Fatemi-Socie fatigue index contour (η=1) of the 162 kN wheel load with elastic material at the sixth loading cycle by searching selected plane at all nodes

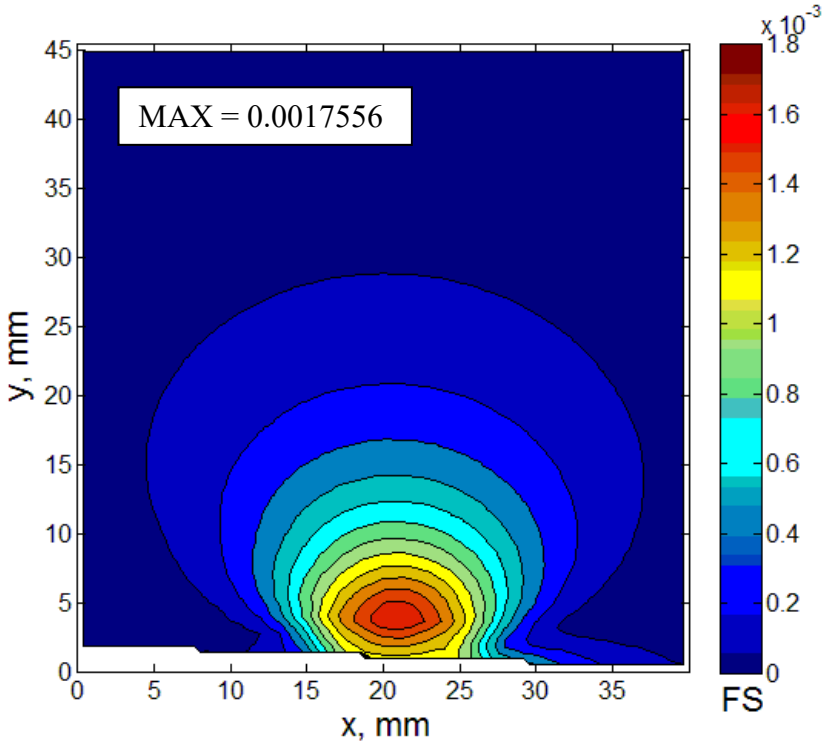

Figure 3.12. Maximum Fatemi-Socie fatigue index contour (η=3) of the 162 kN wheel load with elastic material at the sixth loading cycle by searching selected plane at all nodes

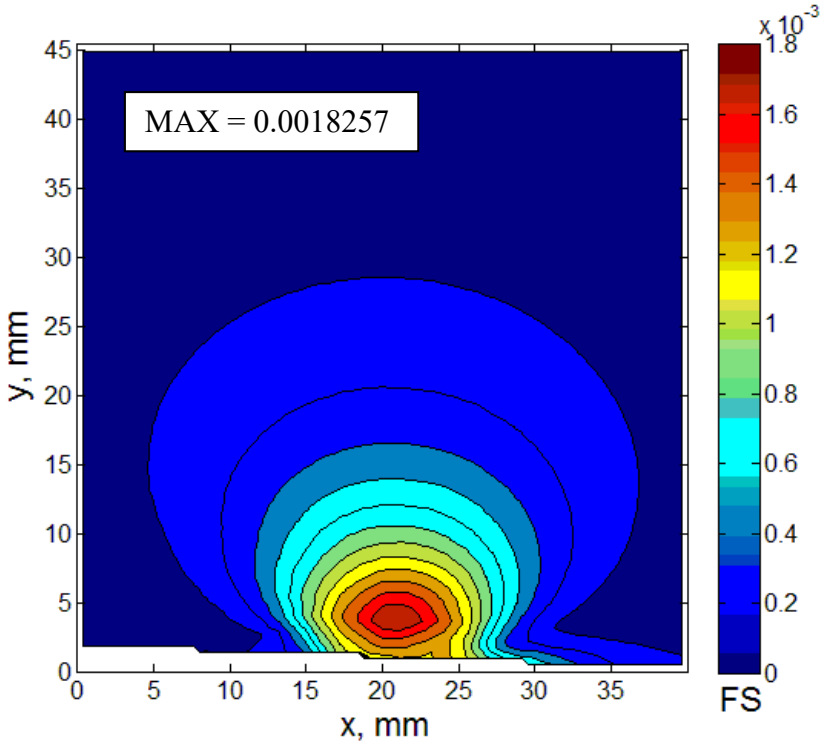

Figure 3.13. Maximum Fatemi-Socie fatigue index contour (η=5) of the 162 kN wheel load with elastic material at the sixth loading cycle by searching selected plane at all nodes

3.4.3 Fatigue Index of the 233 kN Wheel Load with Material Hardening

Figure 3.14, 3.14, 3.15, and 3.16 illustrate the FS fatigue index contours during the sixth cycle of a rolling contact of the 233 kN wheel load as η equals to 0, 1, 3, and 5 respectively. In all cases, fatigue index increased compared to corresponding 162 kN cases with the same depth of crack nucleation site. Multiple fatigue nucleation sites are observed in cases of η equal to 3 and 5. In these cases, the crack nucleation sites in approximate depth of 10-15 mm under the running surface of the wheel are predicted.

The crack nucleation depths, direction cosines of critical planes, and corresponding FS fatigue indices of possible crack nucleation sites for all different normal coefficients (η) are summarized in Table 3.2. Results are qualitatively similar to those from 162 kN wheel load case except for η=1 case which a vertical plane in predicted as critical plane of crack propagation. The more vertical crack propagation plane means the initiated crack reaches the wheel surface in a steeper plane. In other words, it reaches the wheel tread faster hence more imminent wheel failure.

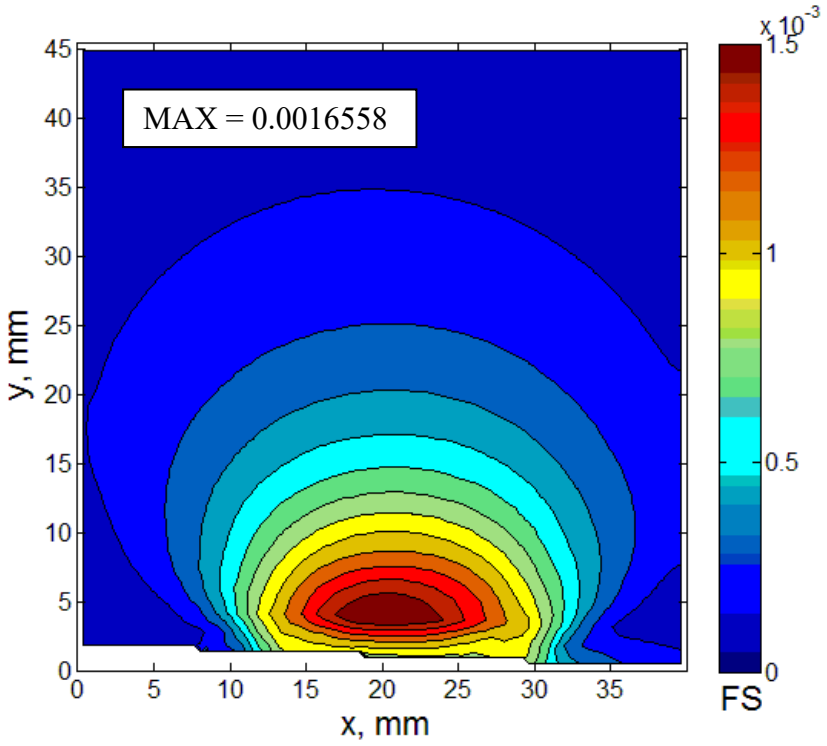

Figure 3.14. Maximum Fatemi-Socie fatigue index contour (η=0) of the 233 kN wheel load with hardening material at the sixth loading cycle by searching selected plane at all nodes

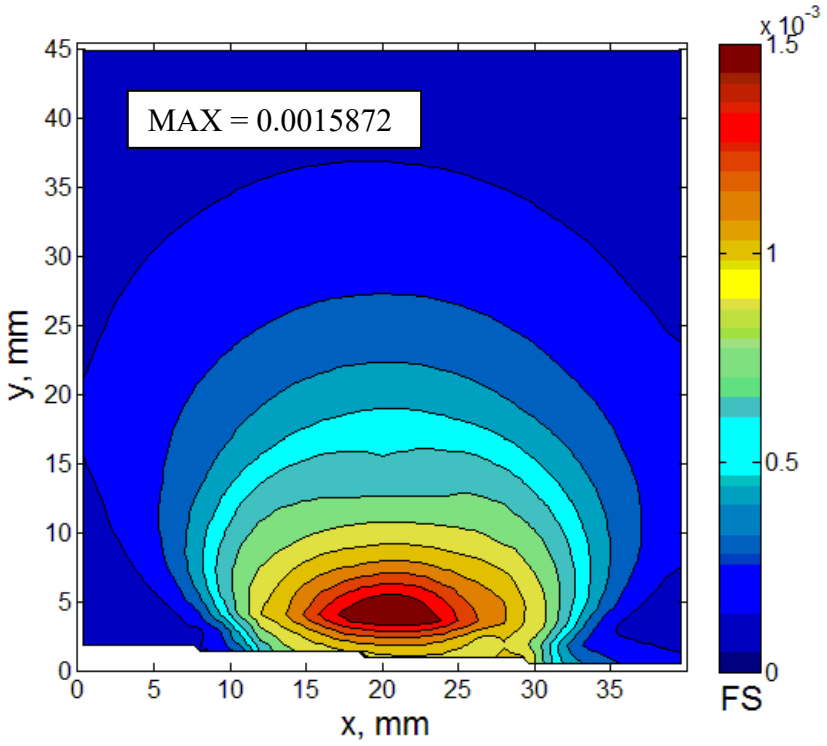

Figure 3.15. Maximum Fatemi-Socie fatigue index contour (η=1) of the 233 kN wheel load with hardening material at the sixth loading cycle by searching selected plane at all nodes

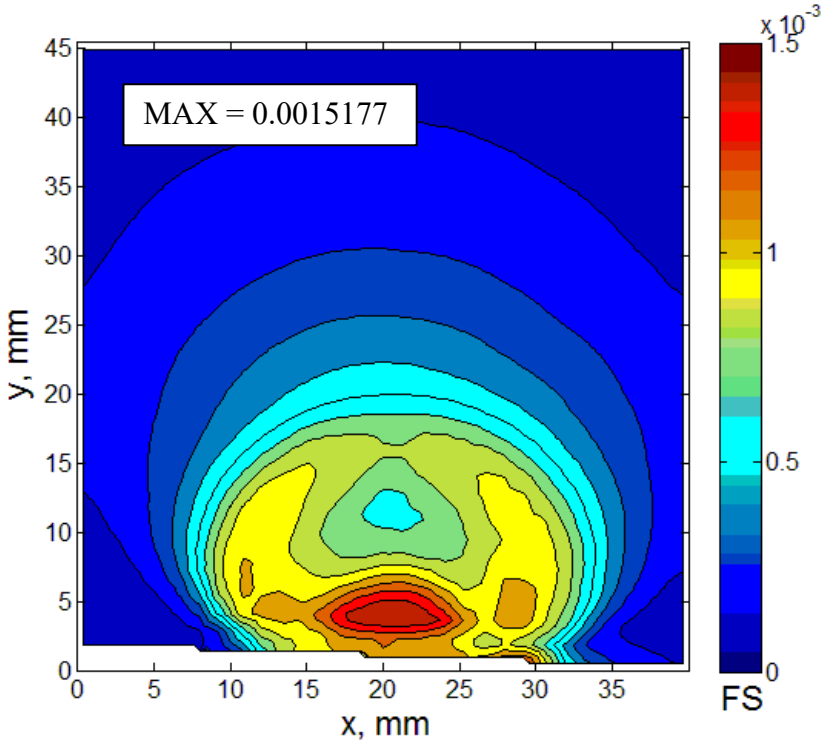

Figure 3.16. Maximum Fatemi-Socie fatigue index contour (η=3) of the 233 kN wheel load with hardening material at the sixth loading cycle by searching selected plane at all nodes

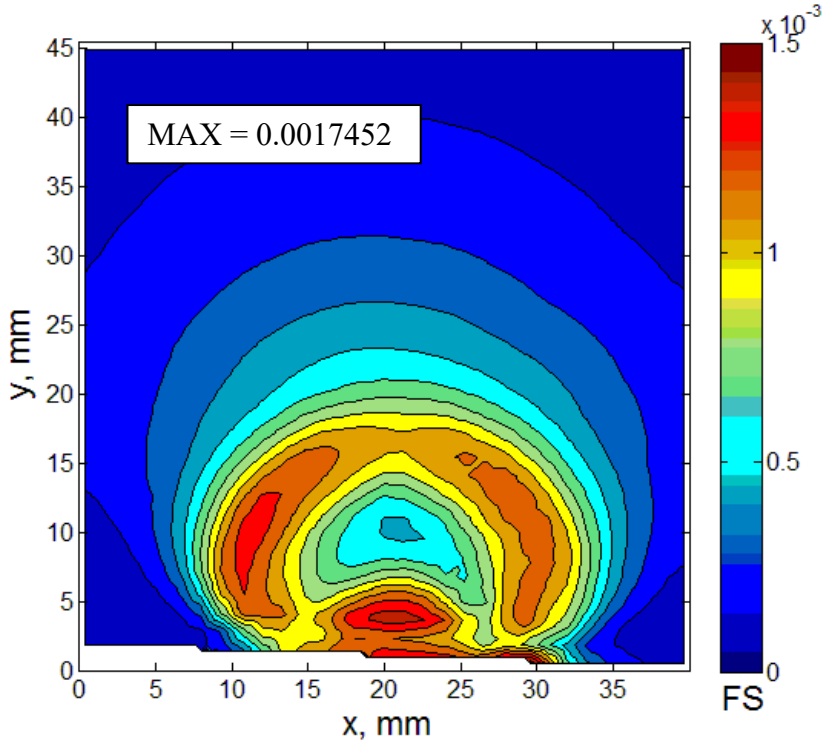

Figure 3.17. Maximum Fatemi-Socie fatigue index contour (η=5) of the 233 kN wheel load with hardening material at the sixth loading cycle by searching selected plane at all nodes

Table 3.2. Summary of possible fatigue crack nucleation sites and cracking planes for the 233 kN wheel load with material hardening and different η values

Normal coefficient (η)	FS fatigue index	Depth below running surface (mm)	Unit normal vector of critical plane			Cracking plane
			x	y	z	
0	0.0016558	3.8	-0.88	-0.32	-0.34	Vertical/Horizontal
1	0.0015872	3.8	-0.97	-0.17	0.17	Vertical
3	0.0015177	3.8	0.49	-0.85	0.17	Horizontal/Vertical
5	0.0017452	0.5	0.00	0.00	-1.00	Transvers

3.4.4 Effect of Wheel Load on Fatemi-Socie Fatigue Index in Cases with Material Hardening

Fatemi-Socie fatigue indexes for 233kN wheel load case are greater than 162 kN wheel load case. In η=5 case that considers more normal stress effect, the crack nucleation sites occur in greater depth when the wheel load increases from 162kN to 233 kN for both near surface and subsurface regimes (Figure 3.8 and Figure 3.17). In both cases, high fatigue indexes on wheel tread observed possibly suggesting the influence of wheel load (normal stresses) on wheel surface fatigue damage.

The predicted crack propagation critical planes are almost similar in both wheel load cases with slight difference in η=1 case. In this case, the critical plane for 233 kN wheel load is predicted to be more inclined to vertical plane. This could be due to higher

tensile residual stresses at subsurface level which may increase the possibility of vertical split rim (VSR) failure in railway wheel subjected to higher wheel loads.

In conclusion, increase of wheel load would increase fatigue damage in wheel tread as well as wheel subsurface. The higher wheel load may increase the possibility of VSR failure.

3.4.5 Effect of Shear Strain Amplitude and Normal Stress Components on Fatemi-Socie Fatigue Index

This section is to study the surface and subsurface fatigue crack nucleation mechanisms of railway wheel. The FS fatigue index in equation (3.1) is decomposed to its two components of shear strain amplitude term of $\frac{\Delta\gamma_{\max}}{2}$ and modified normal stress term of $\frac{\Delta\gamma_{\max}}{2}\left(\eta\frac{\sigma_{n,max}}{\sigma_y}\right)$. Figure 3.18 again shows the Fatemi-Socie fatigue index contour of the 162 kN wheel load ($\eta = 3$) during the sixth loading cycles which is decomposed into the above-mentioned two components presented in Figure 3.19 and Figure 3.20 for shear strain amplitude and modified normal stress, respectively. By comparing Figure 3.18 to 3.19 it can be drawn that the near surface nucleation site agrees with the shear strain amplitude contour, while the subsurface crack nucleation is affected both by shear strain amplitude and normal stress.

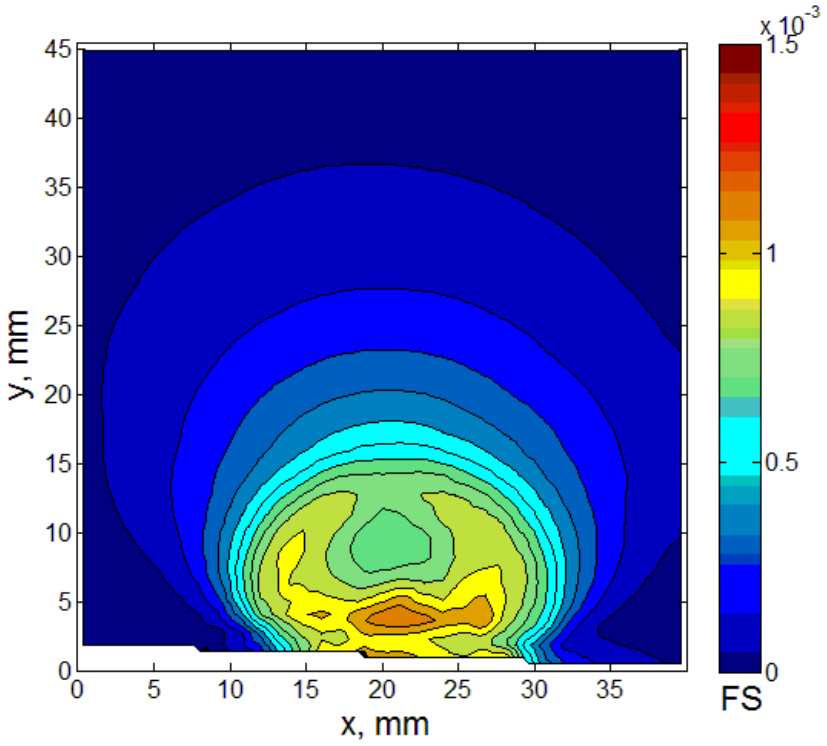

Figure 3.18. Fatemi-Socie fatigue index contours (η = 3) of the 162 kN wheel load at the sixth loading cycle

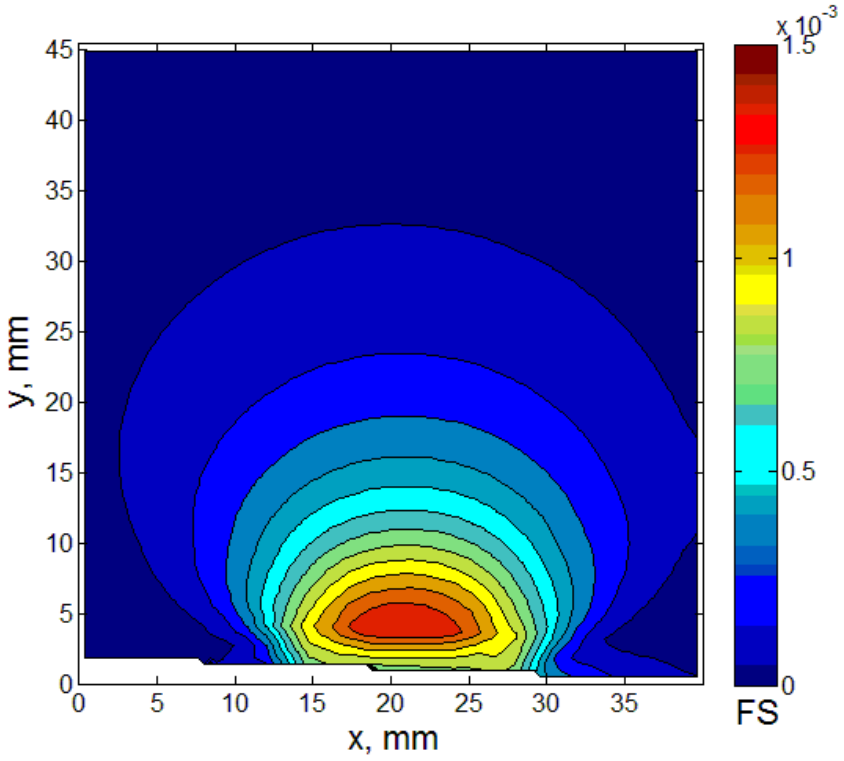

Figure 3.19. Fatemi-Socie fatigue index of its shear strain amplitude contours (η = 3) of the 162 kN wheel load at the sixth loading cycle

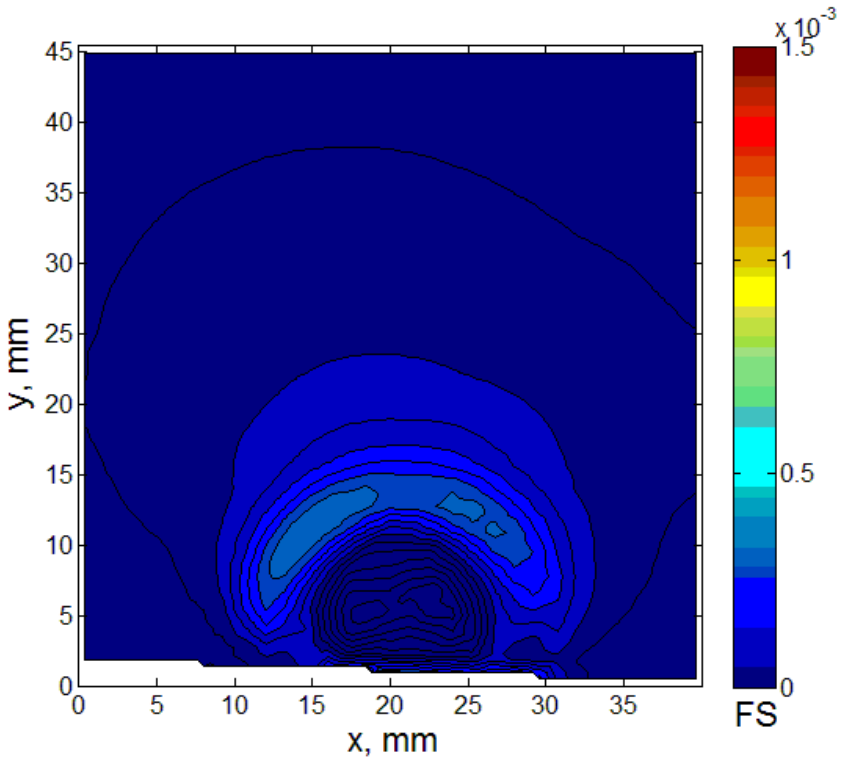

Figure 3.20. Fatemi-Socie fatigue index of its normal stress component contours (η = 3) of the 162 kN wheel load at the sixth loading cycle

3.4.6 Evaluation of η for a Pearlitic Rail Steel

As it's discussed in previous subsections, the initiation of subsurface fatigue cracks depends on the normal stress term which is influenced by η in Fatemi-Socie fatigue criterion. The greater η is, the greater FS fatigue index will be and consequently higher chance of subsurface crack nucleation.

The value of η for perlitic rail steel has been evaluated by Tangtragulwong [39] in a similar study on railheads. He determined η from a regression analysis between the FS fatigue index and fatigue life data of various loading configurations: uni-axial, torsion-axial, and bending, for rail steel and concluded that the proper value of η is the one that gives the best linear fitting of a log-log plot between the FS fatigue index and fatigue life. Figure 3.21 shows the results of the regression analysis for η=1, where the calculated least square error is minimized. Tangtragulwong calculation of η is in agreement with the results reported by Park and Nelson [62] showing that η is varying from 0 to 2 for different types of steel. Jiang, et al. [30] considered 0.98 for S460N steel (Figure 3.22) and also Stephens, et al. [63] recommended η=1 for a first approximation when fatigue test data is not available.

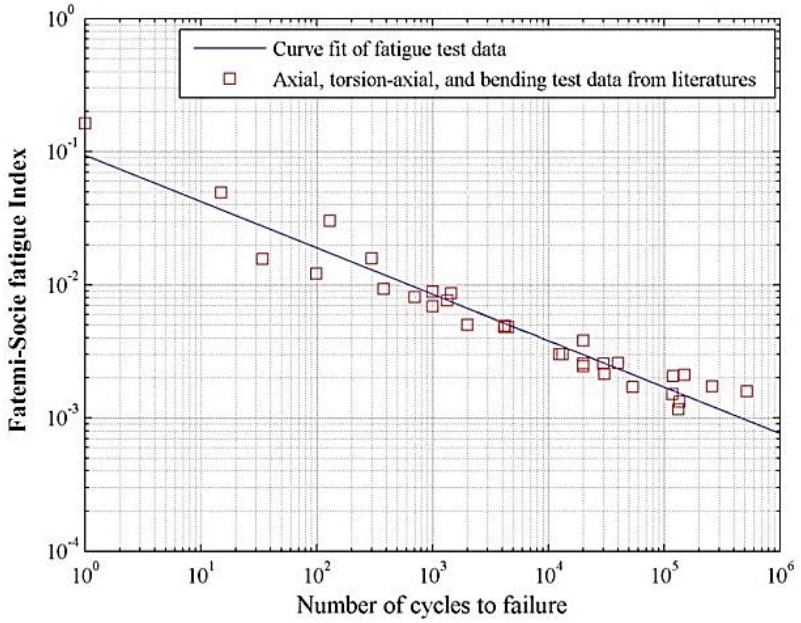

Figure 3.21. A log-log plot between the Fatemi-Socie fatigue index and number of cycles [39]

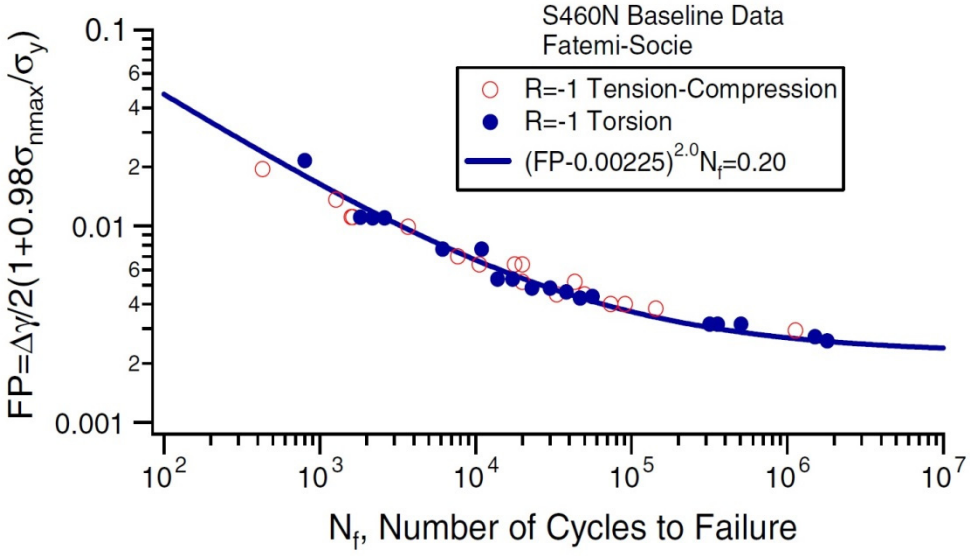

Figure 3.22. Baseline experimental data for determining the fatigue constant η in the FS criterion [30]

3.4.7 Fatigue Life Predictions

Definition of failure is the major source of discrepancy in correlating fatigue life data. No good solution yet exists as to the best failure definition criterion [35]. In majority of the cases, cracks are mitigated before they reach the size that cause catastrophic failures. Still, wheel fatigue may have major operational and economical consequences [2].

There are a lot of factors and different assumptions involved in evaluating the fatigue life of a specimen. For instance, the normal coefficient (η) in FS equation is theoretically not a constant and must vary with fatigue life [32]. Also the number of cycles to failure (N_f) in equation 7 is extremely sensitive to the material cyclic properties. Therefor in this study two fatigue life prediction methods adopted to show and discuss the differences.

By combining equation 3.3 with the low cycle fatigue strain-life relation following equation is proposed by Fatemi and Socie [32]:

$$\frac{\Delta\gamma_{\max}}{2}\left(1+\eta\frac{\sigma_{n,\max}}{\sigma_y}\right)=\frac{\tau'_f}{G}\left(2N_f\right)^{b\gamma}+\gamma'_f\left(2N_f\right)^{c\gamma} \tag{3.3}$$

where τ'_f is fatigue strength coefficient, γ'_f is fatigue ductility coefficient, $b\gamma$ is fatigue strength exponent, $c\gamma$ is fatigue ductility exponent, G is shear modulus, and N_f is number of cycles to failure. Using this equation with material properties of peralitic rail steel from Ringsberg [9], the number of cycles to failure is $N_f = 11{,}000{,}000$; however, using the result of the regression analysis from test data of previous literatures for η=1 the

number of cycles to the first micro-crack nucleation is predicted to be about 220,000 which agrees with the number of cycles to failure from the equation proposed by Jiang, et al. [30] (see Figures 3.21 and 3.22).

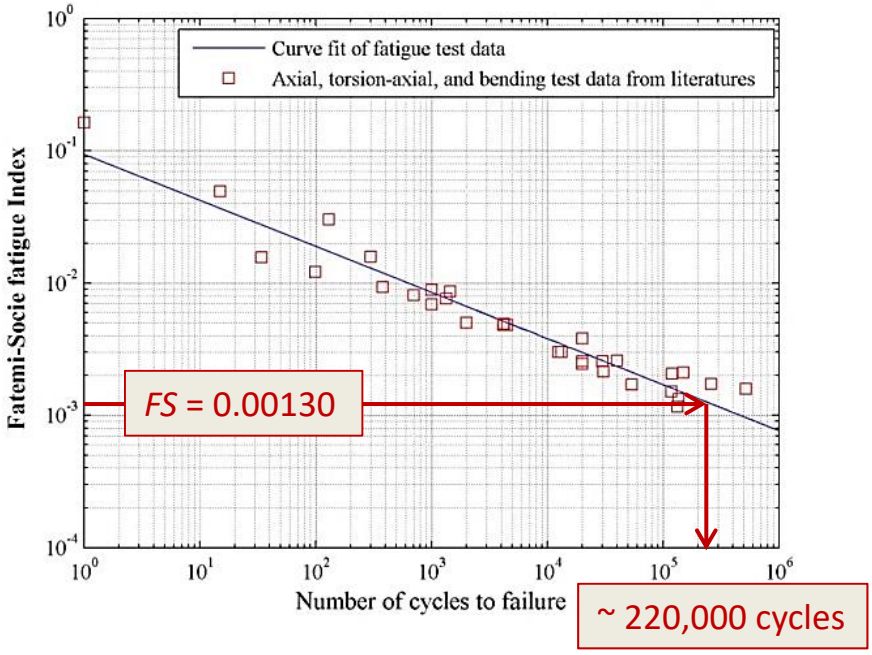

Figure 3.23. Predicted number of cycles to the first micro-crack nucleation based on the data from previous literatures

3.5 Summary

- The observed fatigue index reduction in using hardening material as opposed to elastic material indicates the beneficial role of the strain hardening on subsurface fatigue crack nucleation.
- The predicted crack propagation critical planes are almost similar in both wheel load cases with slight difference in $\eta=1$ case. In this case, the critical plane for 233 kN wheel load is predicted to be more inclined to vertical plane. This could be due to higher tensile residual stresses at subsurface level which may increase the possibility of vertical split rim (VSR) failure in railway wheel subjected to higher wheel loads.
- The near surface nucleation site agrees with the shear strain amplitude contour, while the subsurface crack nucleation is affected both by shear strain amplitude and normal stress which indicates the mixed mode nature of the wheel fatigue failure at subsurface level.
- Considering the recommended value of $\eta=1$ for normal coefficient, the total number of cycles to micro-crack nucleation is around 220,000 which agrees with previous studies.

4 STUDY OF A RAILWAY WHEEL IN PRESENCE OF A PENNY-SHAPED CRACK

4.1 Introduction

The state of stress and strain in the vicinity of a defect subjected to a passing rolling contact is very complex [60]. This section focuses on the influence of a defect at subsurface level of a railway wheel. The FE-simulation of the wheel in presence of a defect shows the change in stress and strain fields at wheel's subsurface level in comparison with the defect-free wheel that presented in section 2.

4.2 Background

Railways provide an effective and reliable transportation method. However, railway systems are very sensitive to defects and in this perspective, rolling contact fatigue (RCF) is a crucial subject that can compromise the integrity of the system [60]. Previous studies [46, 58] have shown how material defects affect the stress and strain fields particularly in the vicinity of the crack tips.

The geometry of penny-shaped cracks is useful in stress analysis since it represents an idealization of the shape of internal defects that are inherent in many engineering materials [64]. Sack [65] and Sneddon [66] are the first ones to studied the 3D aspects of the stress state around a penny-shaped crack.

Broek [67] showed how cracks subjected to multiaxial loading generally grow based on mode I crack propagation path; however, this does not seem to be the case in rolling contact due to a large confining pressures under the contact region. Ekberg [20] explained that in rolling contact cracks propagate in a mixed mode II – mode III and there is a lack of universal criteria to predict the crack growth direction. Bold, et al. [68] argued the complications for simulating mode II propagation in field tests, making it difficult to verify numerical models (see Figure 4.1).

Kabo and Ekberg [60] investigated the influence of defect size of material defects on rolling contact fatigue of railway wheels by quantifying the fatigue impact using Jiang–Sehitoglu multiaxial fatigue criterion. They concluded that semi-empirical methods derived for uniaxial loading are not applicable to rolling contact loading. Instead they designed an elasto-plastic finite element model to compare fatigue impact of defects of different sizes subjected to rolling contact loading.

Kotoul [69] performed a computational 2D analysis of crack path for crack in a railway wheel rim using Plank and Kuhn criterion to decide whether crack would follow mode I path (tensile mode), or it will propagate coplanar mode II (shear mode).

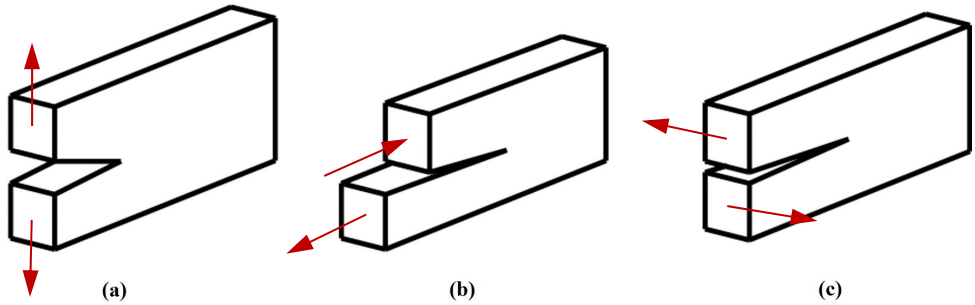

Figure 4.1. The three fracture modes: (a) Mode I: Opening, (b) Mode II: In-plane shear, (c) Mode III: Out-of-plane shear

4.3 FE Modeling of the Wheel in Presence of a Crack

A penny-shaped crack is implemented at the subsurface level of the same wheel/rail model presented in section 2. Sub-modeling technique is employed for accuracy and computational efficiency. The constructed sub-model and the specification of the implemented crack are presented in following subsections.

4.3.1 Sub-modelling

In order to capture local stress/strain field histories in the crack tip, finite element analysis is conducted using the sub-modeling technique in ABAQUS®. First the global model constructed in HyperMesh® is analyzed with ABAQUS®. Considering that HyperMesh does not support ABAQUS® sub-modeling directly, the sub-modeling performed in ABAQUS Keyword Edition®. ABAQUS C3D8R element used which are re-

duced-integration 8-noded elements with three translational degrees of freedom at each node.

Finally, the sub-model is post-processed using HyperView® and ABAQUS/CAE. Figure 4.2 to 4.3 illustrate the location and orientation of the implemented crack as well as the level of mesh refinement and mesh transition between global model and sub-model. Element sizes in global model and sub-model are 2*1.3*1.3 mm^3 and 0.1*0.1*0.1 mm^3, respectively. It's worth mentioning that 3D elastic-plastic RCF analysis is very time-consuming even when using sub-modeling technique.

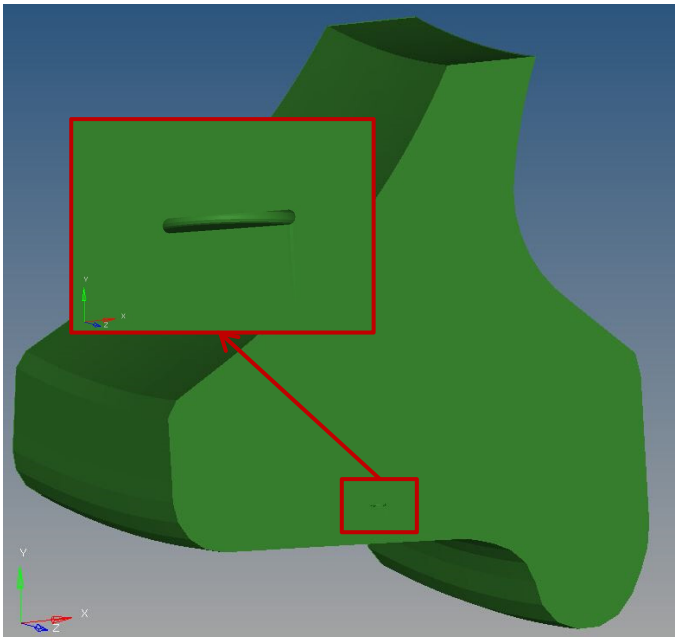

Figure 4.2. Location (10 mm beneath the wheel tread) and orientation (parallel to the wheel tread) of the implemented subsurface crack

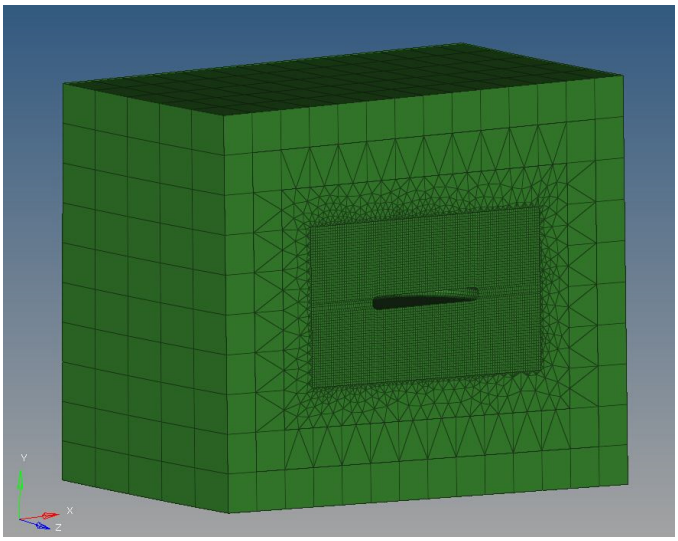

Figure 4.3. Level of mesh refinement and mesh transition between global model and sub-model

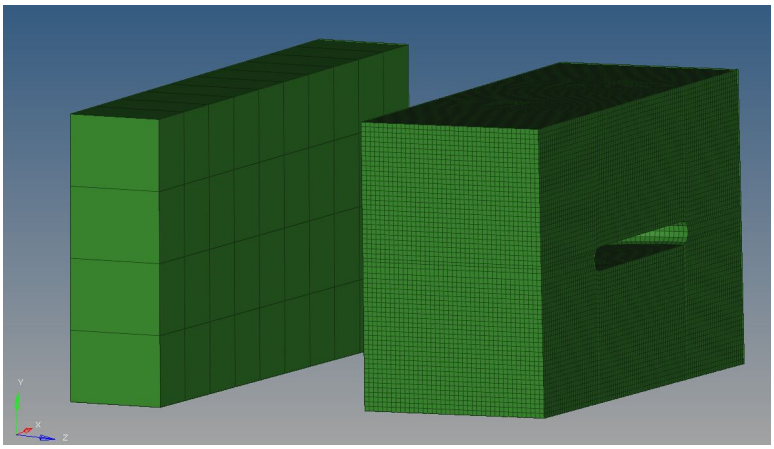

Figure 4.4. Element size comparison between global model (left) and sub-model (right)

4.3.2 Crack Specifications

Following are the specifications of the implemented blunt penny-shaped crack:

- The crack diameter and its thickness are 5 mm and 0.5 mm, respectively (Figure 4.5),
- Round edges with root radius of 0.25 mm considered to overcome stress singularities at the crack-tip,
- HyperMesh solid partitioning feature is employed to achieve proper mapable meshing at the crack region (Figure 4.6).

Figure 4.7 shows the three principal axes (vertical, longitudinal, and transverse) and the position of the crack compared to them (not in scale). The normal stress directions are defined according to these principal axes.

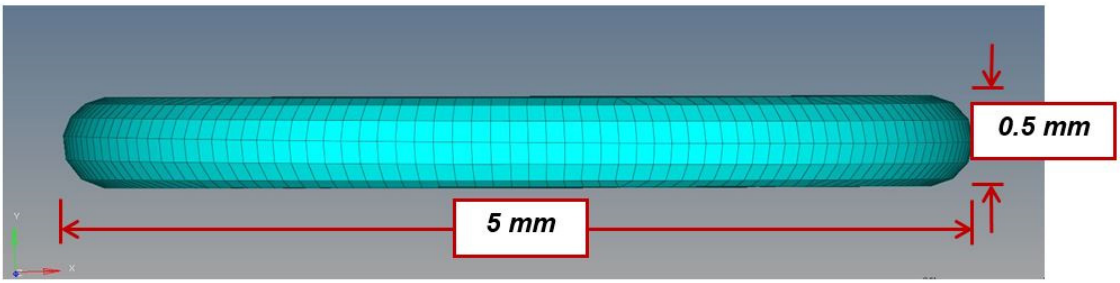

Figure 4.5. Crack dimension

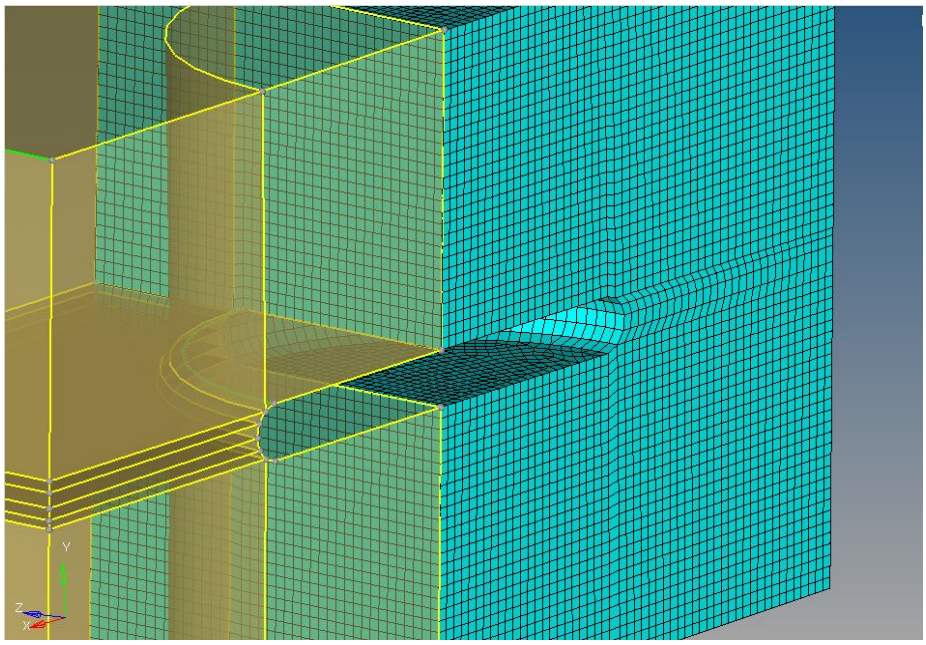

Figure 4.6. Solid partitioning around the crack

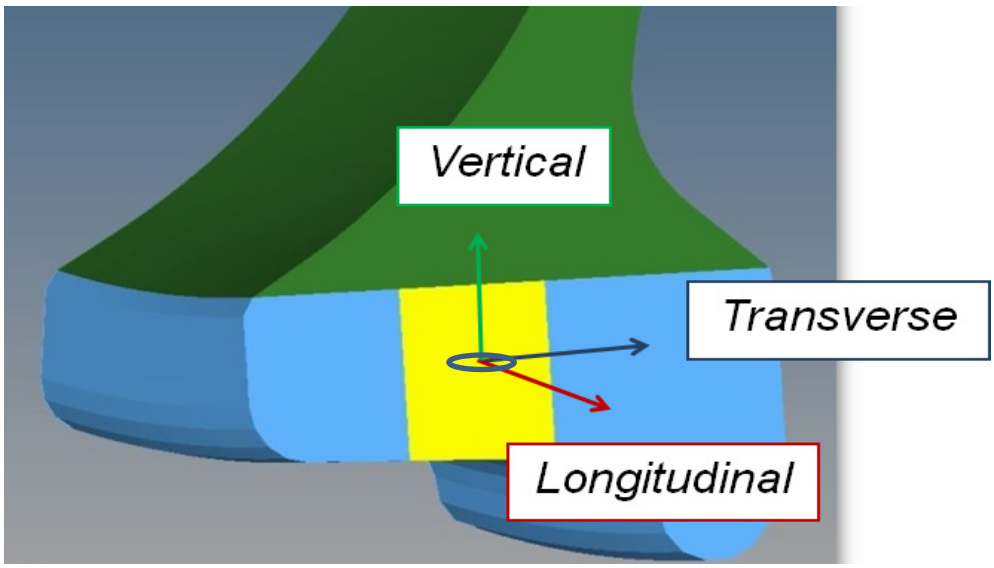

Figure 4.7. Principal axes of interest in a wheel model

4.4 Results and Discussion

In this study, the wheel/rail model with 162 kN load with an implemented defect is analyzed. Different criteria such as von Mises, normal, and shear stress fields around the crack-tip during the wheel revolution are presented and discussed.

4.4.1 The von Mises Stress Evolution around the Crack

Equivalent stress approaches are extensions of static yield criteria to fatigue [63]. One of the most commonly used equivalent stress method for fatigue is the equivalent tensile stress theory (or von Mises theory). The von Mises yield criterion, σ_v, in terms of stress components, is a scalar value that can be computed using equation (4.1):

$$\sigma_v^2 = \frac{1}{2}\left[\left(\sigma_{11}-\sigma_{22}\right)^2+\left(\sigma_{22}-\sigma_{33}\right)^2+\left(\sigma_{33}-\sigma_{11}\right)^2+6\left(\sigma_{23}^2+\sigma_{31}^2+\sigma_{12}^2\right)\right] \qquad (4.1)$$

The cross section of interest is located at the middle – 35 mm from the starting point – of the 70 mm long rolling trajectory. Figure shows the Mises stresses in vicinity of the implemented crack at three different wheel locations: when wheel makes contact with rail and rolling initiates (loading phase), mid-cycle which is when crack is right on top of the contact region (loading ends and unloading begins), and end-cycle which is when a full rolling contact cycle completes (unloading ends). The Mises contours in Figure are not in the same scale instead the values of the Mises stresses are real-time to illustrate the evolution of the stresses at specific times in a full loading cycle.

The equivalent rolling stress is localized around the crack-tip at all three mentioned wheel locations. First when the wheel makes contact – before loading initiates – the maximum von Mises stress is 86 MPa. At the end of loading cycle when the crack is right above the contact region, the stress at crack-tip reaches the pick value of 688 MPa and finally at the end of the full cycle, it reduces to residual stress of 407 MPa. The end-cycle quarter-cut view of the crack shows the higher von Mises residual stresses in transverse plane than vertical plane (see Figure 3.9 for the defined planes).

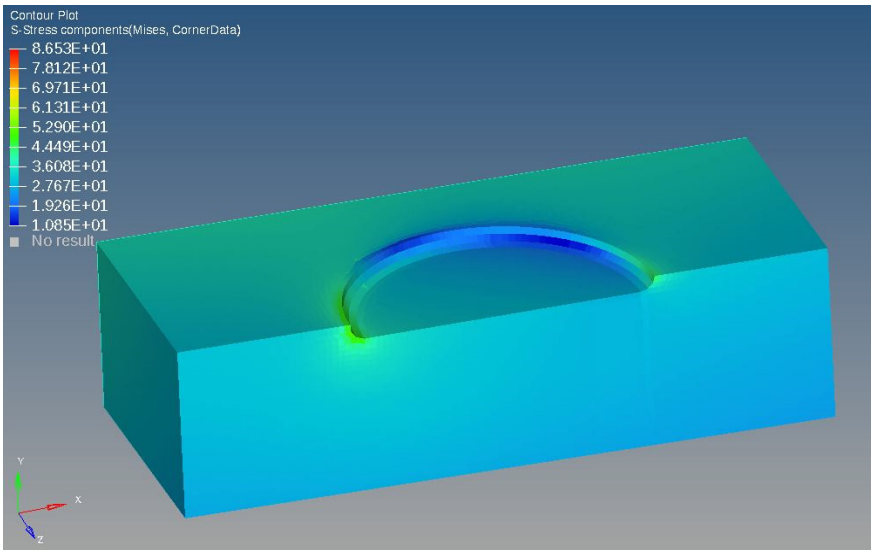

(a)

Figure 4.8. Quarter-cut view of the von Mises rolling stress contours in transverse plane (shown in different scales): (a) before rolling begins, (b) mid-cycle, and (c) end-cycle

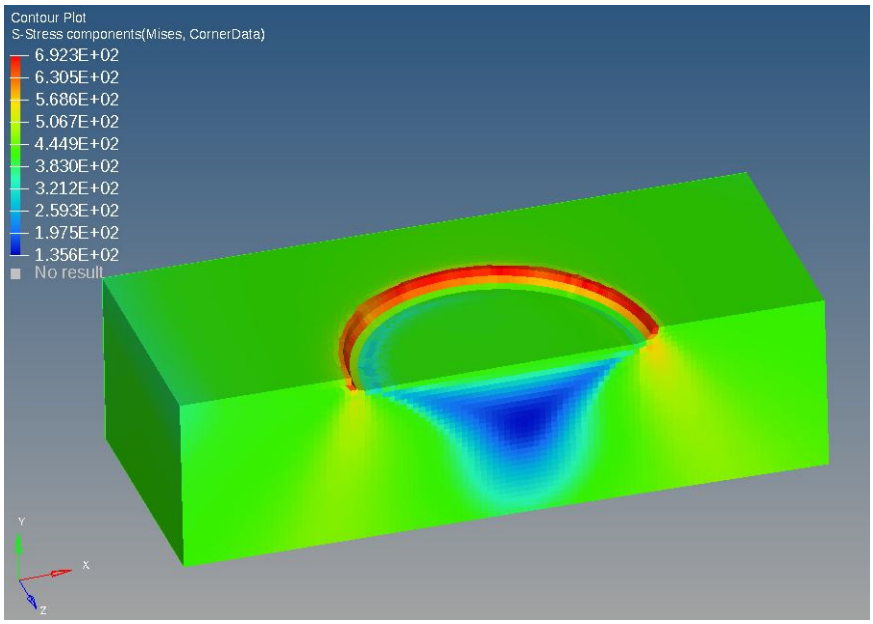

(b)

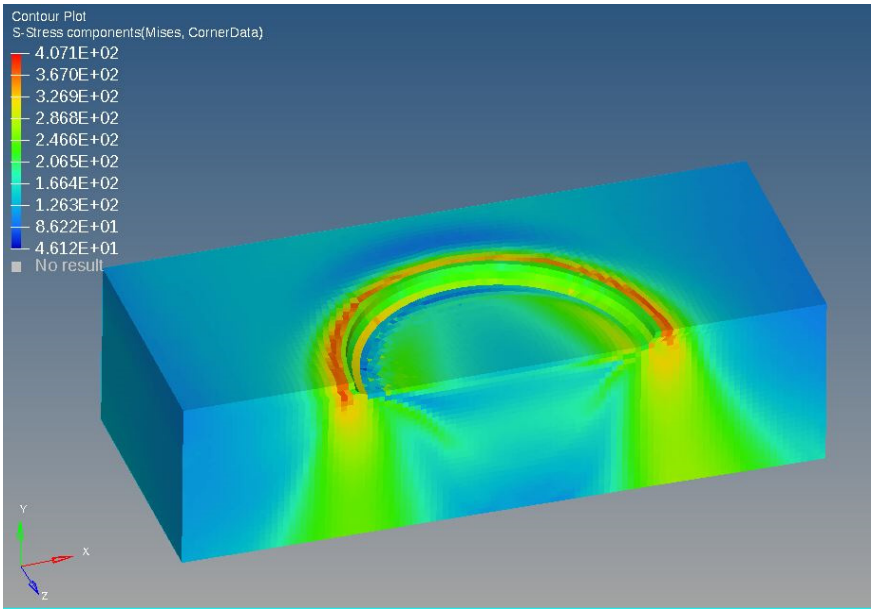

(c)

Figure 4.8. “Continued”

4.4.2 Crack-tip Normal Stress Fields

Figure 4.9 illustrates the normal stress fields around the implemented crack at three loading stages; (a) before rolling begins, (b) mid-cycle which is when the crack is right above the contact region, and (c) end-cycle. The stress fields are in different scales to show the maximum local stresses at each loading stage.

Before loading begins (when wheel is at rest on the rail), the value of normal stresses in all three directions are negligible (with the maximum of 84 MPa for σ_{zz}, longitudinal normal stress). When the wheel reaches mid-cycle (loading ends and unloading begins) the stress field around the crack experiences the maximum of 1,380 MPa for σ_{yy}, vertical normal stress while transverse (σ_{xx}) and longitudinal (σ_{zz}) normal stresses are almost the same value of less than 1,000 MPa compressive at the crack-tip. The high compressive vertical stress is the main reason that the crack would not propagate by the opening mode deformation (Mode I) in rolling contact fatigue. Finally, residual tensile stress is observed at end-cycle which could be in favor of the crack growth at crack-tip region.

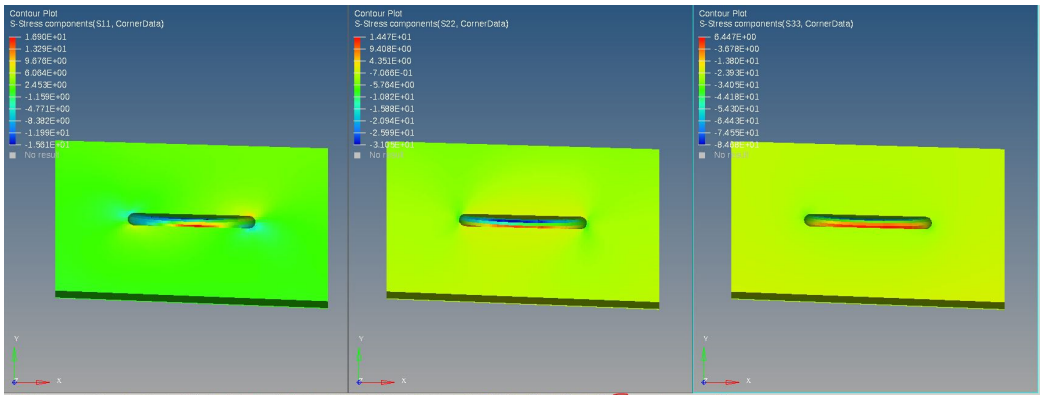

(a)

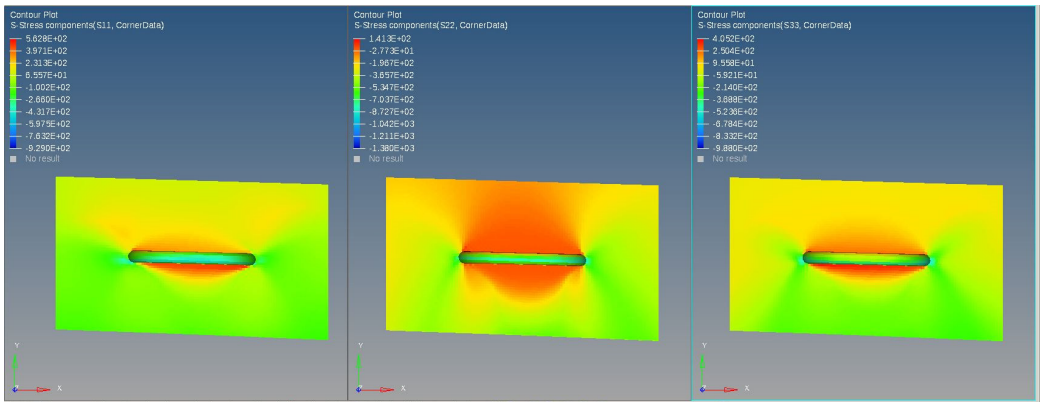

(b)

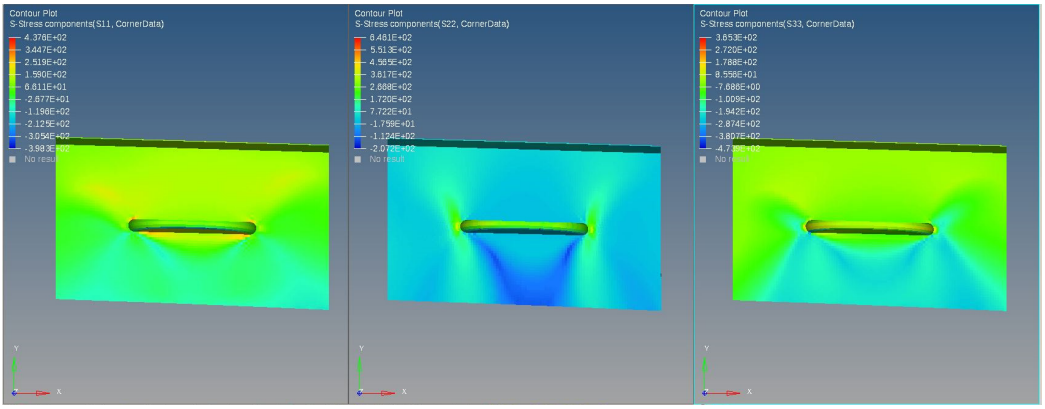

(c)

Figure 4.9. Normal stress components (σ_{xx}, σ_{yy}, and σ_{zz}) in transverse plane: (a) before rolling begins, (b) mid-cycle, (c) end-cycle

4.4.3 Crack-tip Shear Stress Fields

Figure 4.11 shows the shear stress fields around the blunt penny-shaped crack in xy-plane (transverse plane in Figure 3.9). At the beginning of the loading cycle, all the shear stresses are negligible with the maximum of 33 MPa for τ_{yz}. When the crack is right above the contact region (mid-cycle), two crack growth mechanisms can be observed; first in-plane shear mode (Mode II) which is induced by τ_{xy} with the maximum value of 327 MPa and, second out-of-plane shear mode (Mode III) which is induced by τ_{yz} with the maximum value of around 190 MPa in xy-plane. This shows the high possibility of crack growth in mixed-mode II and III.

At the end of the wheel revolution (end-cycle), the higher in-plane shear stress, with the maximum value of 177 MPa, indicates the crack growth mechanism is more inclined to Mode II propagation. Finally, for completeness, τ_{xz} is presented along with the other shear stresses in Figure 4.11.

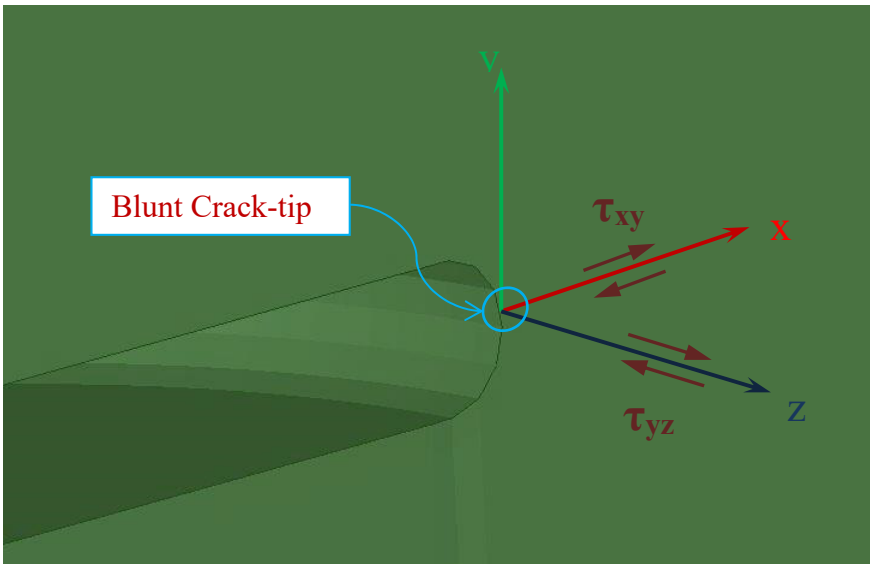

Figure 4.10. Shear stresses at crack-tip: in-plane shear/Mode II (τ_{xy}), out-of-plane shear/Mode III (τ_{yz})

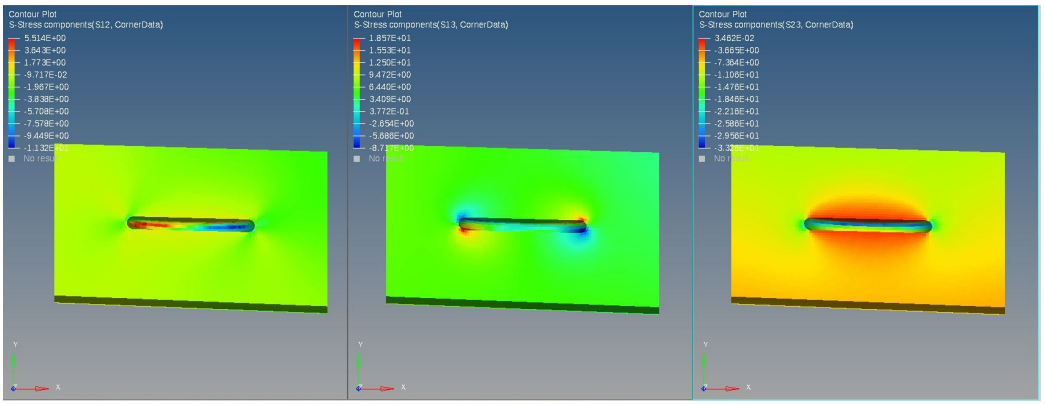

(a)

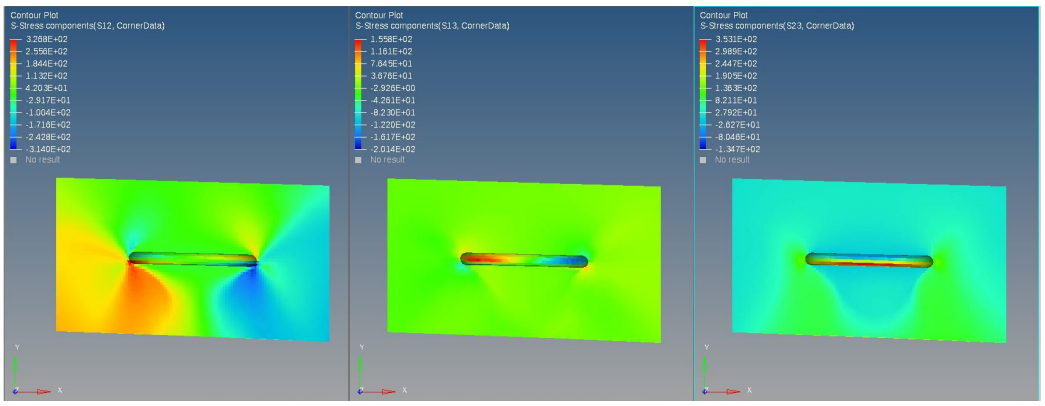

(b)

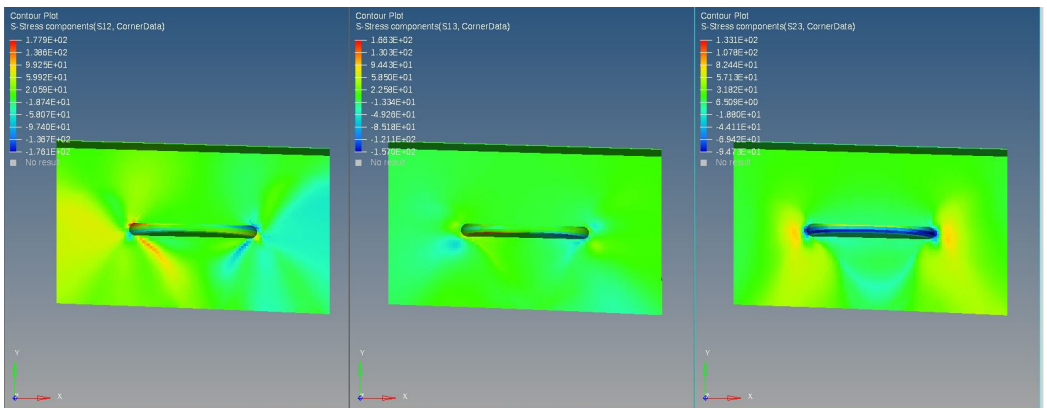

(c)

Figure 4.11. Shear stress components (τ_{xy}, τ_{xz}, and τ_{yz}) in transverse plane: (a) before rolling begins, (b) mid-cycle, (c) end-cycle

4.5 Summary

- The observed von Mises residual stress pattern at the end of the rolling cycle indicates the higher possibility of crack growth in transverse plane.
- The high compressive vertical stress is the main reason that the crack would not propagate by the opening mode deformation (Mode I) in rolling contact fatigue.
- The maximum values of in-plane and out-of-plane shear stresses at crack tip, shows the higher possibility of crack growth in mixed-mode II and III.
- The higher in-plane shear stress at end-cycle indicates the crack growth mechanism for this model is more inclined to Mode II crack propagation.

5 CONCLUSIONS AND FUTURE WORK

5.1 Conclusions

- Profiles of the residual stresses predicted by the Chaboche plasticity model agree well with those from the measurement in literatures; however, to achieve more accurate results, equivalent field tests in accordance with the developed analytical procedure are necessary to calibrate the FE model herein.
- Residual stress reaches the steady-state after fifth loading cycle, showing that the normal components are compressive at closer to tread surface area while they are tensile at deeper region below running surface.
- Wheel subsurface rolling stress history at shallow depth shows lower vertical stress for hardening material case compare to the totally elastic material case whereas the transverse and longitudinal stresses are relatively larger in hardening material case.
- The magnitude of the strain accumulation – and possible subsequent ratchetting of material – is proportional to the wheel load; the more wheel load, the higher strain accumulation is recorded.
- The negative shear strain in vertical plane of yz implies forward flow of material at subsurface level of wheel rim meaning the material flow in the rolling direction. The same phenomenon is reported near running surface of the railhead.

- The observed fatigue index reduction in using hardening material as opposed to elastic material indicates the beneficial role of the strain hardening phenomenon on subsurface fatigue crack nucleation.
- The critical plane for higher wheel load is predicted to be more inclined to vertical plane. This could be due to higher tensile residual stresses at subsurface level which may increase the possibility of vertical split rim (VSR) failure in railway wheel subjected to higher wheel loads.
- The shallow subsurface nucleation site agrees with the shear strain amplitude contour, while the deeper subsurface nucleation site is affected both by shear strain amplitude and normal stress which indicates the mixed mode nature of the wheel fatigue failure at subsurface level.
- Although the maximum values of in-plane and out-of-plane shear stresses at crack tip, shows the higher possibility of crack growth in mixed-mode II and III, the higher in-plane shear stress indicates the crack growth mechanism for this model is more inclined to Mode II crack propagation.

5.2 Suggestions for Future Work

To have a more accurate fatigue life assessment of defect-free railway wheels, factors such as wheel wear and thermal loading due to brake system could be considered. Furthermore, a study of correlation between the predicted fatigue life in this study and the actual fatigue life should be performed.

The applications of fracture mechanics have traditionally concentrated on crack growth problems under an opening or mode I mechanism. However, many service failures occur from growth of cracks subjected to mixed mode loadings. A more in-depth study of different failure mechanisms is necessary to have better understanding of the influence of crack depth and orientation as well as different crack root radius on the fatigue life of railway wheels.

REFERENCES

[1] A. Ekberg and J. Marais, "Effects of imperfections on fatigue initiation in railway wheels," *Journal of Rail and Rapid Transit,* vol. 214, pp. 45-54, 2000.

[2] R. Lewis and U. Olofsson, *Wheel–Rail Interface Handbook*: Woodhead Publishing Limited, 2009

[3] Y. Liu, B. Stratman, and S. Mahadevan, "Fatigue crack initiation life prediction of railroad wheels," *International Journal of Fatigue,* vol. 28, pp. 747-756, 2006.

[4] A. Ekberg and P. Sotkovszki, "Anisotropy and rolling contact fatigue of railway wheels," *International Journal of Fatigue,* vol. 23, pp. 29-43, 2001.

[5] A. Ekberg, E. Kabo, J. C. O. Nielsen, and R. Lundén, "Subsurface initiated rolling contact fatigue of railway wheels as generated by rail corrugation," *International Journal of Solids and Structures,* vol. 44, pp. 7975-7987, 2007.

[6] A. Ekberg, E. Kabo, and H. Andersson, "An engineering model for prediction of rolling contact fatigue of railway wheels," *Fatigue & Fracture of Engineering Materials & Structures (FFEMS),* vol. 25, pp. 899-909, 2002.

[7] S. Bogdanski and M. W. Brown, "Modelling the three-dimensional behaviour of shallow rolling contact fatigue cracks in rails," *Wear,* vol. 253, pp. 17-25, 2002.

[8] J. W. Ringsberg, H. Bjarnehed, A. Johansson, and B. L. Josefson, "Rolling contact fatigue of rails - finite element modelling of residual stresses, strains and crack initiation," *Journal of Rail and Rapid Transit,* vol. 214, pp. 7-19, 2000.

[9] J. W. Ringsberg, "Life prediction of rolling contact fatigue crack initiation," *International Journal of Fatigue,* vol. 23, pp. 575-586, 2001.

[10] J. C. O. Nielsen, A. Ekberg, and R. Lundén, "Influence of short-pitch wheel/rail corrugation on rolling contact fatigue.," *Journal of Rail and Rapid Transit,* vol. 219, pp. 177-187, 2005.

[11] S. L. Grassie, "Rolling contact fatigue on the British railway system: treatment," *Wear,* vol. 258, pp. 1310-1318, 2005.

[12] J. W. Ringsberg, F. J. Franklin, and B. L. Josefson, "Fatigue evaluation of surface coated railway rails using shakedown theory, finite element calculations, and lab and field trials," *International Journal of Fatigue,* vol. 27, pp. 680-694, 2005.

[13] H. Muster, H. Schmedders, K. Wick, and H. Pradier, "Rail rolling contact fatigue. The performance of naturally hard and head-hardened rails in track," *Wear,* vol. 191, pp. 54-64, 1996.

[14] K. Sawley and J. Kristan, "Development of bainitic rail steels with potential resistance to rolling contact fatigue," *Fatigue Fract Engng Mater Struct,* vol. 26, pp. 1019-1029, 2003.

[15] P. J. Webster, X. Wang, G. Mills, and G. A. Webster, "Residual stress changes in railway rails," *Physica B,* vol. 180 & 181, pp. 1029-1031, 1992.

[16] S. Grassie, P. Nilsson, K. Bjurstrom, A. Frick, and L. G. Hansson, "Alleviation of rolling contact fatigue on Sweden's heavy haul railway," *Wear,* vol. 253, pp. 42-53, 2002.

[17] R. A. Smith, "The wheel-rail interface - some recent accidents," *Fatigue and Fracture of Engineering Materials and Structures,* vol. 26, pp. 901-907, 2003.

[18] A. Kapoor, "A re-evaluation of the life to rupture of ductile metals by cyclic plastic strain," *Fatigue Fract Engng Mater Struct,* vol. 17, pp. 201-219, 1994.

[19] V. S. Sura, "Failure modeling and life prediction of railroad wheels," Ph.D. Dissertation, Civil Engineering, Vanderbilt University, Nashville, Tennessee, 2011.

[20] A. Ekberg, "Rolling contact fatigue of railway wheels," Ph.D. Thesis, Department of Solid Mechanics, Ph.D. Thesis, Department of Solid Mechanics, Chalmers University of Technology, Goteborg, 2000.

[21] K. L. Johnson, *Contact mechanics*. Cambridge, UK: Cambridge University Press, 1985.

[22] A. Bernasconi, M. Filippini, S. Foletti, and D. Vanudo, "Multiaxial fatigue of a railway wheel steel under non-proportional loading," *International Journal of Fatigue,* vol. 28, pp. 663-672, 2006.

[23] P. J. Mutton and C. J. Epp, "Rolling contact fatigue in railway wheels under high axle loads," *Wear,* vol. 144, pp. 139-152, 1991.

[24] M. Diener and A. Ghidini, "Materials for heavy haul solid wheels: new experiences," *Journal of Rail and Rapid Transit,* vol. 224, pp. 421-428, 2010.

[25] A. Ekberg and E. Kabo, "Fatigue of railway wheels and rails under rolling contact and thermal loading - an overview," *Wear,* vol. 258, pp. 1288-1300, 2005.

[26] R. Lindqvist, "On high cycle fatigue analyssis of as-cast nodular cast iron components.," Licentiate of Engineering Thesis, Department of Naval Architecture and Ocean Engineering, Licentiate of Engineering Thesis, Department of Naval Architecture and Ocean Engineering, Chalmers University of Technology, Goteborg, 1999.

[27] R. Lundén, "Cracks in railway wheels under rolling load.," presented at the Proc. of the 10th International Wheelset Congress, Sydney, Australia, 1992.

[28] A. Melander, "Effects of hoop and residual stresses on the critical size of inclusions under rolling contact fatigue conditions," presented at the Proc. of the 7th International Fatigue Congress, Beijing, China, 1999.

[29] A. Melander, "Simulations of the behavior of short cracks at inclusion under rolling contact fatigue loading - especially the effect of plasticity.," in *Bearing steels: into the 21st century*, ed: ASTM STP 1327, 1998.

[30] Y. Jiang, O. Hertel, and M. Vormwald, "An experimental evaluation of three critical plane multiaxial fatigue criteria," *International Journal of Fatigue,* vol. 29, pp. 1490-1502, 2007.

[31] K. Dang Van, G. Cailletaud, J. F. Flavenot, A. Le Douaron, and H. P. Lieurade, "Criterion for high cycle failure under multiaxial loading," in *Biaxial and multiaxial fatigue*, ed London, UK: Mechanical Engineering Publications, 1989, pp. 459-478.

[32] D. F. Socie and G. B. Marquis, *Multiaxial fatigue*. Warrendale, PA: Society of Automotive Engineers, 2000.

[33] Y.-L. Lee, M. E. Barkey, and H.-T. Kang, *Metal Fatigue Analysis Handbook*, 1st ed.: Elsevier Inc., 2011.

[34] F. A. Kandil, M. W. Brown, and K. J. Miller, "Biaxial low cycle fatigue fracture of 316 stainless steel at elevated temperatures," in *Proceedings of the International Conference on Mechanical Behaviour and Nuclear Application of Stainless Steels at Elevated Temperatures*, London, 1982, pp. 203-210.

[35] A. Fatemi and D. F. Socie, "A critical plane approach to multiaxial fatigue damage including out-phase loading," *Fatigue & Fracture of Engineering Materials & Structures (FFEMS),* vol. 11, pp. 149–165, 1988.

[36] M. A. Meggiolaro and J. T. P. Castro, "Evaluation of multiaxial stress-strain models and fatigue life prediction methods under proportional loading," in *Mechanics of Solids in Brazil 2009*, H. S. Da Costa Mattos and M. Alves, Eds.,

ed Rio de Janeiro, Brazil: Brazilian Society of Mechanical Sciences and Engineering, 2009.

[37] Y. Liu and S. Mahadevan, "Multiaxial high-cycle fatigue criterion and life predictionfor material.," *International Journal of Fatigue,* vol. 7, pp. 790-800, 2005.

[38] A. F. Bower and K. L. Johnson, "Shakedown, Residual Stress and Plastic Flow in Repeated Wheel-Rail Contact," in *Rail Quality and Maintenance for Modern Railway Operation*, K. J. J., Ed., ed: Kluwer Academic Publishers, 1993, pp. 239--249.

[39] P. Tangtragulwong, "Optimal railroad rail grinding for fatigue mitigation," Ph.D. Dissertation, Department of Civil Engineering, Ph.D. Dissertation, Department of Civil Engineering, Texas A&M University, College Station, TX, 2010.

[40] J. L. Chaboche, "On Some Modifications of Kinematic Hardening to Improve the Description of Ratchetting Effects," *International Journal of Plasticity,* vol. 7, pp. 661-678, 1991.

[41] A. Johansson and H. Thorbemtsson, "Elastoplastic material model with nonlinear kinematic hardening for rolling and sliding contact fatigue," Technical Report EX, 1997.

[42] A. F. Bower, "Cyclic hardening properties of hard-drawn copper and rail steel," *J. of Mech. Phys. Solids,* pp. 455-470, 1989.

[43] Altair, *HyperMesh Tutorials: Abaqus Solver Interface*: Altair Enginnering Inc., 2014.

[44] Simulia, *ABAQUS 6.13 analysis user's manual*. Providence, RI: Dassault Systemes Simulia Corp., 2013.

[45] Y. Jiang and H. Sehitoglu, "Rolling contact stress analysis with the application of a new plasticity model," *Wear,* vol. 191, pp. 35-44, 1996.

[46] E. Kabo and A. Ekberg, "Fatigue initiation in railway wheels - on the influence of defects," *Wear,* vol. 253, pp. 26-34, 2002.

[47] A. T. DeWald, S. Cummings, and J. Punwani, "Measurement of Residual Stress in Railway Wheels With Vertical Split Rim Failure," in *Proceedings of the ASME 2012 Rail Transportation Division Fall Technical Conference*, Omaha, Nebraska, USA, 2012.

[48] C. Lonsdale, J. Oliver, R. K. Maram, and C. S., "Development of Railroad Wheel Rim Axial Residual Stress in Heavy Axle Load Service," in *ASME 2013 Rail Transportation Division Fall Technical Conference*, Altoona, Pennsylvania, USA, 2013.

[49] R. J. Pomeroy and K. L. Johnson, "Residual stresses in rolling contact," *The Journal of Strain Analysis for Engineering Design,* vol. 4, pp. 208-218 1969

[50] M. Shima, K. Okada, Y. Kimura, and T. Yamamoto, "Measurements of subsurface plastic flow in rolling contact," *J JSLE Int Edn,* vol. 2, pp. 75–80, 1981.

[51] G. M. Hamilton, "Plastic flow in rollers loaded above the yield point," in *Proc Inst Mech Eng*, 1963, pp. 667-675.

[52] R. Lundén, "Contact region fatigue of railway wheels under combined mechanical rolling pressure and thermal brake loading," *Wear,* vol. 144, pp. 57-70, 1991.

[53] Y. Jiang, "A fatigue criterion for general multiaxial loading," *Fatigue Fract Engng Mater Struct,* vol. 23, pp. 19-32, 2000.

[54] M. Sraml, J. Flasker, and I. Potrc, "Numerical procedure for predicting the rolling contact fatigue crack initiation," *International Journal of Fatigue,* vol. 25, pp. 585-595, 2003.

[55] Y. B. Guo and M. E. Barkey, "Modeling of rolling contact fatigue for hard machined components with process-induced residual stress," *International Journal of Fatigue,* vol. 26, pp. 605-613, 2004.

[56] A. Bernasconi, P. Davoli, M. Filipini, and S. Foletti, "An integrated approach to rolling contact sub-surface fatigue assessment of railway wheels," *Wear,* vol. 258, pp. 973-980, 2005.

[57] R. Doering, J. Hoffmeyer, T. Seeger, and M. Vormwald, "Short fatigue crack growth under nonproportional multiaxial elastic-plastic strains," *International Journal of Fatigue,* vol. 28, pp. 972-982, 2006.

[58] E. Kabo, "Material defects in rolling contact fatigue of railway wheels - influence of overloads and defect clusters," *International Journal of Fatigue,* vol. 24, pp. 887-894, 2002.

[59] E. Kabo and A. Ekberg, "The influence of defects in rolling contact fatigue," presented at the Proc. of Rolling Contact Fatigue: Applications and Developments, Brescia, Italy, 2002.

[60] E. Kabo and A. Ekberg, "Material defects in rolling contact fatigue of railway wheels - the influence of defect size," *Wear,* vol. 258, pp. 1194-1200, 2004.

[61] J. Bannantine, *Fundamentals of metal fatigue analysis*: Prentice Hall, 1990.

[62] J. Park and D. Nelson, "Evaluation of an energy-based approach and a critical plane approach for predicting constant amplitude multiaxial fatigue life," *International Journal of Fatigue,* vol. 22, pp. 23–39, 2000.

[63] R. I. Stephens, A. Fatemi, R. R. Stephens, and H. O. Fuchs, *Metal fatigue in engineering*, 2nd ed. New York, NY: Wiley-Interscience, 2000.

[64] G. C. Sih, *Handbook of stress intensity factors*. Bethlehem, Pennsylvania: Institute of Fracture and Solid Mechanics, Lehigh University, 1973.

[65] R. A. Sack, "Extension of Griffith's theory of rupture to three dimensions," in *Proceedings of Physical Society*, London, 1946.

[66] I. N. Sneddon, "The distribution of stress in the neighbourhood of a crack in an elastic solid," in *Proc. Roy. Soc.*, London, 1946.

[67] D. Broek, *The practical use of fracture mechanics*. Dordrecht, Netherlands: Kluwer Academic Publishers, 1989.

[68] P. E. Bold, M. W. Brown, and R. J. Allen, "Shear mode crack growth and rolling contact fatigue," *Wear,* vol. 144, pp. 289-306, 1991.

[69] M. Kotoul, "Crack path modelling in railway wheel under rolling contact fatigue," *Applied and ComputationalMechanics,* vol. 9, pp. 103–126, 2015.